J.-S. Lönnroth, V. Parail, G. Huysmans, G. Saibene, H. Wilson, S. Sharapov, G. Corrigan, D. Heading, R. Sartori, M. Bécoulet, and JET-EFDA contributors. 2004. Predictive transport modelling and MHD stability analysis of mixed type I-II ELMy H-mode JET plasmas. Plasma Physics and Controlled Fusion, volume 46, number 5, pages 767-796.

http://www.iop.org/journals/ppcf
http://stacks.iop.org/ppcf/46/767

INSTITUTE OF PHYSICS PUBLISHING PLASMA PHYSICS AND CONTROLLED FUSION

Plasma Phys. Control. Fusion **46** (2004) 767–796 PII: S0741-3335(04)70395-4

Predictive transport modelling and MHD stability analysis of mixed type I-II ELMy H-mode JET plasmas

J-S Lönnroth[1], V Parail[2], G Huysmans[3], G Saibene[4], H Wilson[2], S Sharapov[2], G Corrigan[2], D Heading[2], R Sartori[4], M Bécoulet[3] and JET-EFDA contributors

[1] Association EURATOM-Tekes, Helsinki University of Technology, PO Box 2200, 02015 HUT, Finland
[2] EURATOM/UKAEA Fusion Association, Culham Science Centre, Abingdon, Oxfordshire OX14 3DB, UK
[3] Association EURATOM-CEA, CEA Cadarache, DRFC, 13108 Saint-Paul-Lez-Durance, France
[4] EFDA Close Support Unit, c/o Max Planck Institut für Plasmaphysik, Boltzmannstrasse 2, 85748 Garching, Germany

Received 14 October 2003
Published 26 March 2004
Online at stacks.iop.org/PPCF/46/767
DOI: 10.1088/0741-3335/46/5/004

Abstract
Mixed type I-II ELMy H-mode, a mode operation with small, frequent type II edge localized modes (ELMs) interrupted by occasional large type I ELMs, has been observed in various experimental situations. This paper combines two simple models for type I and type II ELMs, respectively (used e.g. in Lönnroth *et al* 2003 *Plasma Phys. Control. Fusion* **45** 1689) into an improved scheme for modelling of mixed type I-II ELMy H-mode, which has been implemented in the 1.5D core transport code JETTO together with simple schemes for modelling of pure type I and type II ELMy H-modes based on the same ideas. In the ELM modelling, transport during the ELMs is enhanced by edge-localized radially Gaussian-shaped perturbations to the transport coefficients. Type I and type II ELMs are represented by perturbations with different widths and amplitudes and controlled by different stability limits derived from magnetohydrodynamic (MHD) stability analysis. Some justification from theory and numerical analysis is given for the representation of each ELM type. Predictive transport simulations with JETTO demonstrate that the experimental dynamics of mixed type I-II ELMy H-mode can be qualitatively reproduced using the present model. For completeness, the modelling of mixed type I-II ELMy H-mode is compared with reference simulations of pure type I and pure type II ELMy H-mode and the differences, e.g. in confinement are explained. In addition, this paper presents the results of MHD stability analysis of a number of situations experimentally found to be favourable for the occurrence of type II ELMs, namely situations with strong external neutral gas puffing, a quasi-double-null magnetic configuration, high poloidal β (ratio of the total pressure to the kinetic

pressure) and combinations of high edge safety factor q_{95} and high triangularity δ. The results of the analysis of the given scenarios are such that the model used in this paper can explain why these situations can be favourable for mixed type I-II or pure type II ELMy H-mode.

(Some figures in this article are in colour only in the electronic version)

1. Introduction

The high confinement mode (H-mode) offers a promising operational regime for tokamak fusion devices. A characteristic feature of the H-mode is the formation of an edge transport barrier (ETB) in the outer region of the plasma, just inside the magnetic separatrix. The reduction of transport within the ETB leads to large density and temperature gradients in this region, causing it to stand out as a 'pedestal' in the density and temperature profiles. The H-mode is generally accompanied by short periodic bursts of particles and energy at the plasma edge triggered by magnetohydrodynamic (MHD) instabilities and known as edge localized modes (ELMs). There are several effects of ELMs on plasma performance. ELMs have the beneficial effect of transporting density and impurities over the pedestal region. ELM-free plasmas usually terminate due to the accumulation of impurities, because particles and especially impurities are extremely well confined in them. However, the ELM-related energy loss, although only a small fraction of the total plasma energy, can produce high peak heat loads on the divertor plates, which can become a serious problem in large tokamaks. Another effect of ELMs is to limit the pressure gradient within the pedestal and at the top of it, thereby affecting confinement.

Different ELM types have been identified or defined. Type I or 'giant' ELMs are the most commonly observed type of ELMs in plasmas with large enough heating power. They are large events capable of removing up to 10% of the plasma energy with a repetition frequency that increases with increased radial power flux across the last closed flux surface. Type III ELMs, which are small and frequent, are often seen slightly above the H-mode threshold power. Type II ELMs resemble type III ELMs, but are generally even tinier and more frequent. Sometimes MHD activity in type II ELMy H-mode has a continuous rather than an intermittent character. Type III ELMs are generally characterized by an ELM frequency that decreases with power [1]. Another distinction between ELM types II and III, both of which are commonly referred to as 'grassy ELMs', is based on their different effects on plasma performance. Generally, type II ELMs do not seriously reduce plasma confinement, whereas type III ELMs are associated with a significant deterioration of plasma confinement, compared to type I ELMy H-mode. Type II ELMs often occur in a mixed type I-II ELMy H-mode regime, i.e. in a mode of operation with tiny, frequent type II ELMs interrupted by occasional, large type I ELMs [2, 3].

Frames (*a*), (*b*) and (*c*) in figure 1 show the characteristic D_α emission signal as a function of time of three different ELMy H-mode JET discharges: 53298, which is a pure type I ELMy H-mode discharge; 53299, which is a mixed type I-II ELMy H-mode discharge and 52739, which is a pure type III ELMy H-mode discharge. Pure type II ELMy H-mode has never been observed at JET. The different levels of confinement associated with type I, type II and type III ELMs are illustrated in frame (*d*) in figure 1, which shows the confinement factor H98Y [4] as a function of time for the three aforementioned discharges.

This paper focuses on plasmas with mixed type I-II ELMs and, to some extent, on pure type II ELM plasmas. Type II ELMs have the advantage of producing much smaller heat and particle loads on the divertor plates than type I ELMs, while still offering good confinement properties. The energy lost in a single type II ELM is significantly smaller than in a single

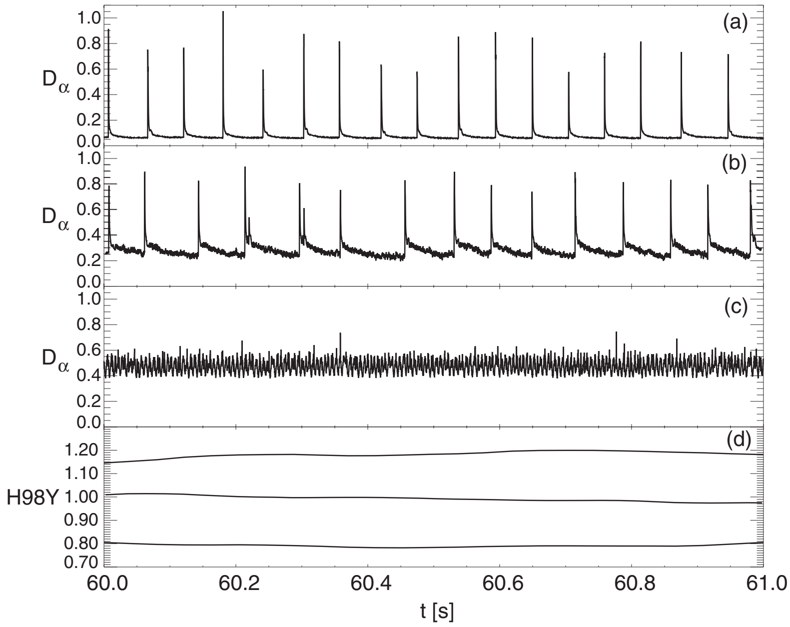

Figure 1. Time traces of $D_{\tilde{\alpha}}$ emission in three JET discharges: (*a*) 53298, which is a pure type I ELMy H-mode discharge. (*b*) 53299, which is a mixed type I-II ELMy H-mode discharge. (*c*) 52739, which is a pure type III ELMy H-mode discharge. Frame (*d*) shows the confinement factor H98Y as a function of time in same three discharges: 53298 (upper curve), 53299 (middle curve) and 52739 (lower curve).

type I ELM, which means that the pulsed power exhaust due to type I ELMs can be completely avoided in operation with pure type II ELMs. Type II ELMy H-mode operation can thus potentially help to solve the problem of too strong an erosion of the divertor and strike point regions—one of the remaining concerns about H-mode operation in future tokamaks.

First, simple models for type I and type II ELMs are introduced. The models make use of the often expressed idea that type I ELMs are associated with medium-n ballooning or peeling modes and type II ELMs with high-n ballooning modes [5–7] and have previously been used in transport simulations in [8]. Here, the ELM models for type I and type II ELMs are combined to define an improved scheme for the modelling of mixed type I-II ELMy H-mode. During the ELMs, transport is enhanced by edge-localized radially Gaussian-shaped perturbations to the transport coefficients. Type I and type II ELMs are controlled by different stability limits derived from MHD stability analysis. The two ELM types are modelled with perturbations having different widths and amplitudes. Some justification from theory and numerical analysis is given for the representation of each ELM type. Simpler schemes based on the same ideas are used for modelling of pure type I and type II ELMy H-mode in reference simulations against which the modelling of mixed type I-II ELMy H-mode is compared. The latter part of this paper presents the results of MHD stability analysis of a number of situations experimentally found to be favourable for the occurrence of type II ELMs, namely situations with strong external neutral gas puffing, a quasi-double-null magnetic configuration, high poloidal β (ratio of the total pressure to the kinetic pressure) and combinations of high edge safety factor q_{95} and high triangularity δ. The results of the analysis are interpreted in light of the ELM models used in this paper.

It should be noted that the ELM models used here are phenomenological *ad hoc* models with many free parameters, thereby easily capable of qualitatively reproducing the experimental dynamics of various types of ELMy H-mode as well as reproducing, e.g. the right level of confinement and the correct plasma profiles. In various studies, many other schemes have been used in ELM modelling. Recently, for instance, the mode amplitude and onset of ELMs have been self-consistently calculated in simulations of type I ELMy H-mode [9]. To extend such a scheme to modelling of mixed type I-II ELMy H-mode would, however, require the development of a suitable theory-motivated model for type II ELMy H-mode and integration of this model with the model for type I ELMy H-mode. This is left for future work.

2. Occurrence of type II ELMs

Pure type II ELMy H-modes and/or mixed type I-II ELMy H-modes have been observed in several different situations. Perhaps the best example in JET is the occurrence of type II ELMs in discharges with moderately strong gas puffing. From experiments, it is known that plasma easily accommodates modest gas puffing, e.g. a neutral influx of $\Gamma = 3 \times 10^{22}\ \mathrm{s}^{-1}$ in the case of JET. Higher levels of gas puffing can trigger a transition from pure type I ELMy H-mode to mixed type I-II ELMy H-mode and eventually a transition to pure type III ELMy H-mode [10]. The transition from the type I to type III ELM regime is accompanied by a dramatic increase in the ELM frequency and a deterioration of plasma confinement. Strong gas puffing is associated with high edge density, which seems to be a common feature in other scenarios with type II ELM also. Pure type II ELMy H-modes as well as mixed type I-II ELMy H-modes have been observed in plasmas with high poloidal beta β_p in JT-60U [11]. Like high edge density, high β_p seems to be a common feature of discharges with type II ELMs. At JT-60U, high β_p is a necessary condition for access to type II ELM regimes, so that if $\beta_p < 1.7$ there is no access to type II ELMs. Pure type II and mixed type I-II ELMy H-modes have also been observed in JT-60U discharges with high safety factor q at the edge and high triangularity δ [12, 13]. Mixed type I-II ELMy H-modes typically occur for $q_{95} \gtrsim 4$ and $\delta \gtrsim 0.3$ and pure type II ELMy H-modes for $q_{95} \gtrsim 5$ and $\delta \gtrsim 0.45$ in JT-60U. Here, q_{95} is the safety factor at the magnetic surface $\psi = 0.95$, where ψ is the poloidal flux co-ordinate. Pure type II ELMy H-modes as well as mixed type I-II ELMy H-modes have been observed in ASDEX Upgrade in quasi-double-null discharges [14, 15], i.e. in discharges with a magnetic configuration having a second X-point in the proximity of the separatrix. Type II ELMs in quasi-double-null configurations have been reported for a rather broad range of triangularities and edge safety factors, especially at high densities.

3. Simulation codes

In this paper, transport simulations of the time evolution of the plasma parameters have been carried out using the 1.5D JETTO transport code [16] equipped with a new ELM model. The codes HELENA and MISHKA [17] have been used for MHD stability analysis.

3.1. JETTO

In simulations with JETTO, the empirical JET transport model, a mixed Bohm/gyro-Bohm model [18], has been used. The model also includes neoclassical transport from NCLASS [19]. JETTO has a fixed boundary solver of the Grad–Shafranov equation called ESCO, which generates equilibria consistent with the predicted temperature and pressure profiles in the core. JETTO explicitly takes the region with the ETB into account. It is assumed that ion anomalous transport is suppressed within the ETB, so that the only remaining transport is neoclassical. Accordingly, all transport coefficients are reduced to a constant level from the top of the ETB to the plasma edge. Specifically, the electron thermal diffusivity is set equal to the ion thermal diffusivity, which, in turn, is equal to the neoclassical ion thermal diffusivity at the top of the ETB. This means that electron anomalous transport is not fully suppressed, but is kept on a level equalizing it with ion neoclassical thermal diffusivity. The assumption of uniformity of ion neoclassical transport within the ETB is a reflection of the fact that the pedestal width is usually of the order of the ion orbit width, implying limited variation of neoclassical transport across the barrier. The width of the ETB can be considered either a fixed parameter or be calculated using recently developed theory-based models [20]. In this work, a fixed ETB width of 3 cm is used. The effect of letting the pedestal width vary is studied in [21].

3.2. MHD stability codes

In the work presented in this paper, MHD stability analysis has been carried out using the codes HELENA and MISHKA. HELENA takes plasma profiles and equilibrium information generated by JETTO and evaluates stability against ideal $n = \infty$ ballooning modes. HELENA also produces an equilibrium with better resolution, which can then be used by MISHKA as input. MISHKA evaluates stability against finite-n kink, peeling and ballooning modes. For efficiency, a version of the MISHKA code called MISHKA-1 has been used in this paper. This is an ideal MHD version of MISHKA that does not take into account drift effects.

4. Definition of type I and type II ELMs exemplified by simulations differing with respect to the level of external neutral gas puffing

It is broadly believed that ELMs are controlled by a combination of ballooning and peeling modes [7, 22–25]. The definitions of type I and type II ELMs used in this paper are related to the different ballooning stability limits associated with high- and medium-n ballooning modes in different regions of parameter space. These definitions will be explained by considering two predictive transport simulations differing with respect to the level of external neutral gas puffing, each representing a qualitatively different situation with regard to MHD stability. Transitions between these situations are interpreted as transitions between different types of ELMy H-mode. This subject has already been extensively discussed in [8], but some of the results will be reviewed here, because they illustrate how type I and type II ELMs are defined in the present model and because one of the most common situations with type II ELMs is in plasmas with modest to high neutral gas puffing and associated high edge density.

External neutral gas puffing affects MHD stability through a sequence of causalities: due to poor penetration of neutrals through the scrape-off layer (SOL), an increase in gas puffing leads to an increase in the edge density, which in turn results in an increase in the collisionality at the edge. As a consequence of increasing collisionality at the edge, the bootstrap current decreases. A decrease in the bootstrap current causes an increase in magnetic shear at the edge, which directly influences MHD stability.

Figure 2 shows MHD stability diagrams for two different magnetic surfaces, $\rho = 0.95$ and $\rho = 0.99$, for a predictive JETTO simulation with no external neutral gas puffing ($\Gamma = 0$). Here, $\rho = 0.95$ corresponds to a location just outside the top of the ETB and $\rho = 0.99$ to a location just inside the separatrix. Each diagram indicates the mode number of the most unstable kink, peeling or finite-n ballooning mode ($n \leqslant 14$), as well as infinite-n ballooning instabilities, at a number of locations in an operational space with the normalized pressure gradient $\tilde{\alpha}$ on the horizontal axis and magnetic shear s on the vertical axis. In this paper, the

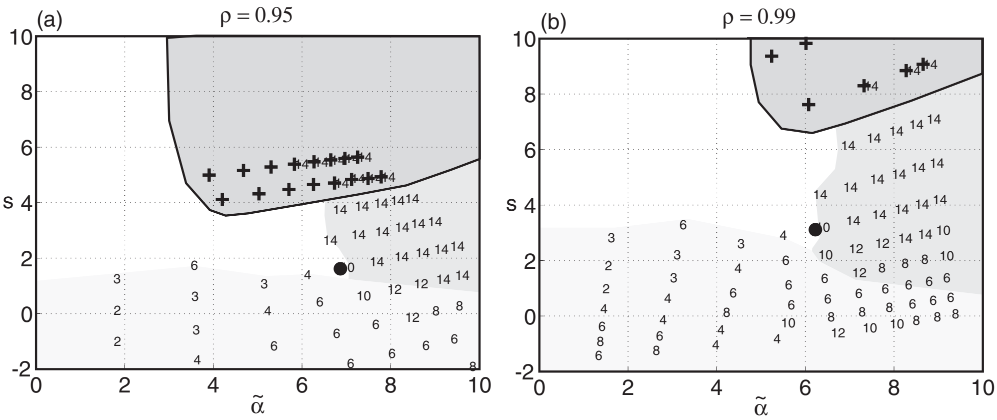

Figure 2. MHD stability diagrams for the magnetic surfaces (*a*) $\rho = 0.95$ and (*b*) $\rho = 0.99$ in a predictive JETTO simulation with no external neutral gas fuelling ($\Gamma = 0$). The numbers on the plot indicate the mode number of the most unstable kink, peeling or ballooning mode. The infinite-*n* ballooning unstable region has been marked with crosses and the operational point with a solid circle.

following definition is used for $\tilde{\alpha}$:

$$\tilde{\alpha} = -\frac{2\mu_0 q^2}{B_0^2 \epsilon}\frac{\mathrm{d}p}{\mathrm{d}\rho}. \tag{1}$$

Here, μ_0 is the permeability of vacuum, q the safety factor, B_0 the magnetic field on the magnetic axis, ϵ the inverse aspect ratio, p the pressure and $\rho = \sqrt{\Phi/(\pi B_0)}$ is the toroidal flux co-ordinate, where Φ is the toroidal flux. In predictive simulations, the plasma profiles, e.g. density, temperature and current, are calculated subject to boundary conditions using the given transport model. Hence, the calculated states cannot be associated with, e.g. any particular ELM in an actual discharge. Here, the predictive JETTO runs have been performed using the geometry of the high triangularity ($\delta = 0.5$) JET discharge 53298. The plasma has been allowed to evolve freely towards a steady state without imposing MHD stability limits on it. MHD stability analysis has been carried out when the pressure gradient just outside the top of the ETB has reached a level roughly corresponding to the finite-*n* ballooning stability limit. For the MHD stability analysis, a suite consisting of the HELENA and MISHKA codes has been used. The codes have been run on a series of equilibria obtained by repeatedly changing the edge pressure gradient and edge current within the ETB. To be specific, the pressure gradient and current profiles have been multiplied by constant multiplication factors in the region between the top of the ETB and the separatrix and these multiplication factors have systematically been varied. Each combination of edge pressure gradient and edge current translates into a given combination of $\tilde{\alpha}$ and s as a function of the flux surface. The plots feature four distinct regions, each of which has been marked with a different shade of grey: a region with no instabilities, a region in which the low n ($n \lesssim 8$) kink instability is dominant, a region in which the medium n ($8 \lesssim n \lesssim 14$) ballooning/peeling instability dominates and the $n = \infty$ ballooning unstable region. In most cases, the latter two regions partially overlap each other. Finally, the plots show the location of the operational point, i.e. the point with unperturbed edge current and edge density.

It should be noted that the operational point is located in the second $n = \infty$ ballooning stability region for both $\rho = 0.95$ and $\rho = 0.99$ in figure 2. In fact, the situation is qualitatively

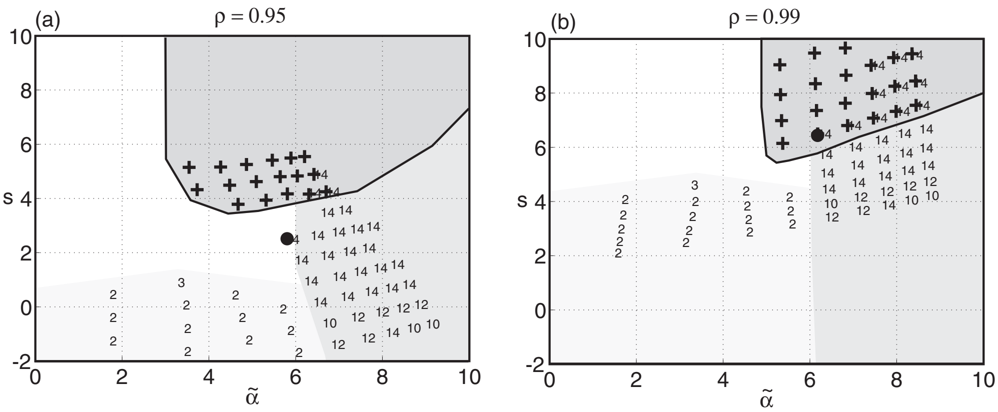

Figure 3. MHD stability diagrams similar to the ones in figure 2 for the magnetic surfaces (*a*) $\rho = 0.95$ and (*b*) $\rho = 0.99$ in a predictive JETTO simulation with an external neutral gas fuelling rate of $\Gamma = 4 \times 10^{22}\ \mathrm{s}^{-1}$.

the same for all magnetic surfaces within the ETB, as can be inferred from the two plots in the figure. Even though the magnetic shear increases close to the separatrix, the operational point stays in the second ballooning stability region even there. The maximum operational $\tilde{\alpha}$ is defined by the finite-n ballooning stability limit at $\tilde{\alpha} \approx 6$. An ELM is triggered when the pressure gradient exceeds this limit. To be specific, an ELM resulting from a violation of the finite-n ballooning stability limit is defined as a type I ELM in the model used in this paper. Consequently, the situation shown in figure 2 corresponds to a pure type I ELMy H-mode.

Figure 3 is similar to figure 2 and contains MHD stability diagrams for the magnetic surfaces $\rho = 0.95$ and $\rho = 0.99$ for a predictive JETTO simulation with an external gas puffing rate of $\Gamma = 4 \times 10^{22}\ \mathrm{s}^{-1}$. In this case, the operational point is located in the second ballooning stability region for $\rho = 0.95$ and in the infinite-n ballooning unstable region for $\rho = 0.99$. More generally, flux surfaces close to the top of the ETB are second ballooning stable, but the outermost flux surfaces just inside the separatrix are infinite-n ballooning unstable. This means that stability at the very edge is defined by the first $n = \infty$ ballooning stability limit, whereas stability deeper inside the ETB is still determined by the finite-n ballooning instabilities. The relevant stability limits are the first ballooning stability limit at $\tilde{\alpha} \approx 3.5$ for the very edge and the finite-n ballooning stability limit at $\tilde{\alpha} \approx 6$ for the rest of the ETB. According to the present model, type I ELMs result from violations of the finite-n ballooning stability limit in the inner part of the ETB. However, violations of the first ballooning stability limit at the outermost flux surfaces are interpreted to result in type II ELMs at the edge. Therefore, the situation shown in figure 3 corresponds to a mixed type I-II ELMy H-mode. More generally, type II ELMs are proposed to be controlled by edge localized high-n ballooning modes rather than by infinite-n ballooning modes only. As will be shown in section 6, ballooning modes become very edge localized in the high-n limit.

Analogously, a pure type II ELMy H-mode is proposed to occur when the pressure gradient in the inner part of the ETB never builds up to the critical level defined by the finite-n ballooning stability limit, but the outermost edge is still unstable against high-n ballooning modes. The high ELM frequency of type II ELMs is explained by the facts that the critical pressure gradient defined by the first ballooning stability limit is relatively small and that type II ELMs are very small perturbations which do not cause the pressure gradient to relax very much.

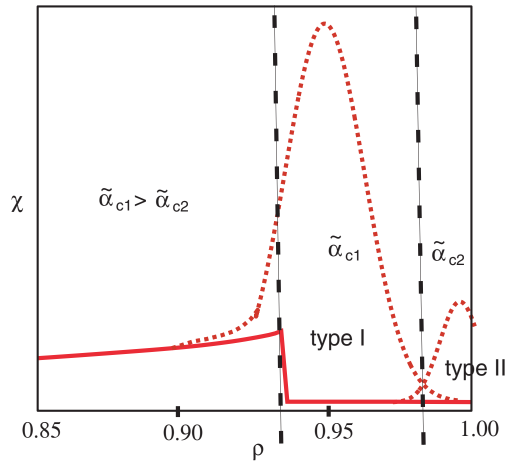

Figure 4. A schematic illustration of the implementation of the model for mixed type I-II ELMy H-mode in JETTO. The ETB has divided into two regions, a narrow edge region for type II ELMs and a wider inner region for type I ELMs. In the two regions, different critical pressure gradients are applied and transport is enhanced by Gaussian-shaped perturbations with different amplitudes, widths and centres.

5. Simulation model for ELMs

Based on the model described in the preceding section, a new implementation for dynamic modelling of mixed type I-II ELMy H-mode has been included in the JETTO transport code. It is assumed that the ELMs are driven by ballooning modes controlled mainly by the edge pressure gradient. An ELM is triggered when the critical pressure gradient defined by an MHD stability limit is exceeded. To a certain extent, the model still implicitly takes into account the edge current also as a mechanism controlling the ELMs, since finite-n ballooning modes are to some extent driven also by the current and this is taken into account when the stability limits are determined using the MISHKA code.

Figure 4 shows a schematic illustration of the implementation of the ELM model. As discussed in the preceding section, a mixed type I-II ELMy H-mode requires separate stability limits for the outermost and the inner regions of the ETB. In accordance with this, the ETB has been divided into two regions in the implementation of the ELM model. In the inner region, the critical pressure gradient is set at a value $\tilde{\alpha}_{c,\mathrm{I}}$ defined by the finite-n ballooning stability limit, typically $\tilde{\alpha}_{c,\mathrm{I}} \approx 6$, whereas in the outer region it is set at a value $\tilde{\alpha}_{c,\mathrm{II}}$ defined by the first ballooning stability limit, typically $\tilde{\alpha}_{c,\mathrm{II}} \approx 3$. The location of the boundary between the two regions can be chosen arbitrarily and is typically set at $\rho = 0.99$. When the critical pressure gradient $\tilde{\alpha}_{c,\mathrm{I}}$ is exceeded in the inner region of the ETB, an ELM having the characteristics of a type I ELM is triggered. Similarly, the system responds with a perturbation corresponding to a type II ELM, when the critical pressure gradient $\tilde{\alpha}_{c,\mathrm{II}}$ is exceeded in the outer region.

In both cases, the ELMs are represented by Gaussian-shaped perturbations added on top of the unperturbed radial profiles of the transport coefficients in the pedestal and its vicinity. The use of Gaussian-shaped ELMs is motivated by the fact that the eigenfunctions of the MHD modes supposed to drive the ELMs usually have Gaussian shapes in linear theory. With this choice of perturbation profile for the ELMs, the perturbed transport coefficient profile $\chi(r)$, where χ stands for ion or electron thermal conductivity or particle diffusivity and r is the radial co-ordinate, can be written as

$$\chi(r) = \chi_0(r) + A\exp\left[-\left(\frac{r-r_0}{\Delta r}\right)^2\right]. \tag{2}$$

Here, $\chi_0(r)$ is the unperturbed transport coefficient profile corresponding to an inter-ELM state, A is the amplitude of the Gaussian-shaped perturbation, r_0 is the radial location of the centre of the perturbation and Δr is the characteristic width of the perturbation. The parameters A, r_0 and Δr are typically chosen rather differently in the representations of type I and type II ELMs. The current understanding is that the infinite- and high-n ballooning modes assumed to determine the stability of the outermost edge region are much more localized than the finite-n ballooning modes assumed to control stability deeper inside the ETB. Some justification for this will be given in the next section. In this ELM model, the perturbation in the outer region is, therefore, typically a very narrow Gaussian centred close to the separatrix, whereas the inner region of the ETB uses a wider Gaussian centred a little further towards the top of the ETB. In other words, $\Delta r_{\mathrm{I}} > \Delta r_{\mathrm{II}}$ and $r_{0,\mathrm{I}} < r_{0,\mathrm{II}}$, where the subscripts I and II on the ELM parameters refer to type I and type II ELMs (or the inner and outer ETB region), respectively, and r increases when moving from the plasma centre towards the edge. In order to account for the experimental observation that type I ELMs are much larger events than type II ELMs, expelling much more particles and energy, the perturbation in the inner pedestal region is usually given a much larger amplitude than the perturbation in the outer region, i.e. $A_{\mathrm{I}} \gg A_{\mathrm{II}}$, the subscripts again referring to type I and type II ELMs.

Typically, the ELMs are ramped up and down over short time intervals, i.e. the ELM amplitude A varies with time t during the ELMs as follows:

$$A(t) = \begin{cases} \dfrac{A_0}{t_2 - t_1}(t - t_1), & t_1 \leqslant t < t_2, \\ A_0, & t_2 \leqslant t \leqslant t_3, \\ \dfrac{A_0}{t_4 - t_3}(t_4 - t), & t_3 < t \leqslant t_4. \end{cases} \tag{3}$$

Here, $t_1 < t_2 < t_3 < t_4$ are times defining the beginning and the end of the ramp-up and ramp-down phases of the ELM and A_0 is the maximum ELM amplitude. The total ELM duration $t_{\mathrm{ELM}} = t_4 - t_1$ is typically around 1 ms and the flat-top phase $t_2 \leqslant t \leqslant t_3$, about half of that. Different maximum amplitudes $A_{\chi_i}(t)$, $A_{\chi_e}(t)$ and $A_D(t)$ can be defined for ion thermal conductivity, electron thermal conductivity and particle diffusivity.

As outlined in this section, the implementation of the ELM model for mixed type I-II ELMy H-mode features a large number of arbitrary free parameters. In simulations, these parameters are generally chosen in such a way that the individual ELMs remove the right amount of heat and particles consistent with experiments and so that the ELM frequency corresponds to experimental observations. Usually, the amplification factor for the particle diffusivity is chosen to be smaller than those for the thermal conductivities in order to avoid excessive flattening of the density profile within the ETB, not consistent with experimental observations.

6. Type II ELM width

In the ELM model for mixed type I-II ELMy H-mode, the type II ELMs are assumed to be controlled by very edge-localized infinite- or high-n ballooning modes. The understanding that the high-n ballooning modes limiting stability near the very edge are more localized for strong magnetic shear than the finite-n ballooning modes determining stability closer to the top of the ETB can be analytically justified as follows. Reference [26] gives an expression for the width W of the envelope of coupled harmonics forming a ballooning mode eigenfunction in the high-n limit with the maximum pressure gradient at the plasma edge:

$$W(x) = \exp\left[-\frac{1}{2}|v'(\theta_0)|\left(\frac{\partial^2\omega^2/\partial\psi^2}{\partial^2\omega^2/\partial\theta_0^2}\right)^{1/2} x^2\right]. \tag{4}$$

Here, $|v'(\theta_0)| = |\mathrm{d}q/\mathrm{d}\psi| = |q'|$ is the derivative of the safety factor with respect to the poloidal flux co-ordinate ψ, ω^2 is the local oscillation frequency of an individual harmonic, θ_0 is the poloidal location of the instability and $x = n^{1/2}(\psi - \psi_0)$, where ψ_0 is the location of the minimum of ω^2 in terms of the poloidal flux co-ordinate. Assuming that $\partial^2\omega^2/\partial\theta_0^2 \sim \omega^2$ and $\partial^2\omega^2/\partial\psi^2 \sim \omega^2/(\Delta\psi_{\mathrm{ETB}})^2$, where $\Delta\psi_{\mathrm{ETB}}$ is the pedestal width, the envelope width can be written as

$$W(\psi) = \exp\left[-\frac{1}{2}\frac{nq'}{\Delta\psi_{\mathrm{ETB}}}(\psi - \psi_0)^2\right]. \tag{5}$$

The width of the envelope $\Delta\psi_{\mathrm{envelope}}$ thus scales as

$$\Delta\psi_{\mathrm{envelope}} \sim \sqrt{\frac{\Delta\psi_{\mathrm{ETB}}}{nq'}}. \tag{6}$$

This shows that ballooning modes become very localized in the high-n limit and for strong magnetic shear at the edge. It should be noted that a $\Delta\psi_{\mathrm{envelope}} \sim (nqs)^{-2/3}a$ scaling, where a is the minor radius at the separatrix, has also been proposed for edge ballooning modes [23]. Recent numerical work, however, suggests a $\Delta\psi_{\mathrm{envelope}} \sim n^{-1/4}a$ scaling for low- and medium-n ballooning modes, which means that these modes usually occupy the whole pedestal [27].

Numerically, the localization and width of high-n ballooning modes has been studied using MISHKA. It has been determined how the mode width varies when the inner part of the pedestal is second ballooning stable and the outer part infinite-n ballooning unstable and the widths of these two regions are changed. The analysis shows that ballooning modes become very narrow and edge localized in the high-n limit, if a significant part of the pedestal is second ballooning stable and only the outermost edge is infinite-n ballooning unstable. Figure 5 illustrates the result for $n = 40$. By perturbing the edge current, the part of the pedestal being second ballooning stable has been varied. Frame (*a*) shows the eigenfunction for a situation in which the edge current is half of that in the original unperturbed equilibrium. This makes the edge infinite-n ballooning unstable from $\psi = 0.935$ to $\psi = 1.000$. The width of the eigenfunction is comparable to the width of the pedestal. In frame (*b*), the edge current is 1.5 times higher than in the original unperturbed equilibrium. Here, the pedestal is infinite-n ballooning unstable only from $\psi = 0.990$ to $\psi = 1.000$. In this case, the eigenfunction is almost as narrow as the unstable region and centred close to the edge of the plasma. It should be noted that [28] reports similar edge localization for low-n peeling-ballooning modes in situations with type II ELMs in ASDEX Upgrade.

7. Results of JETTO modelling

This section describes a number of predictive JETTO transport simulations making use of the ELM modelling scheme presented in section 5. All simulations use the magnetic configuration of JET discharge 53298, a typical type I ELMy H-mode discharge. The toroidal magnetic field is $B_0 = 2.67$ T on the magnetic axis in all the simulations and the total current is $I = 2.5$ MA, as in the original discharge. The external heating power and the boundary conditions for

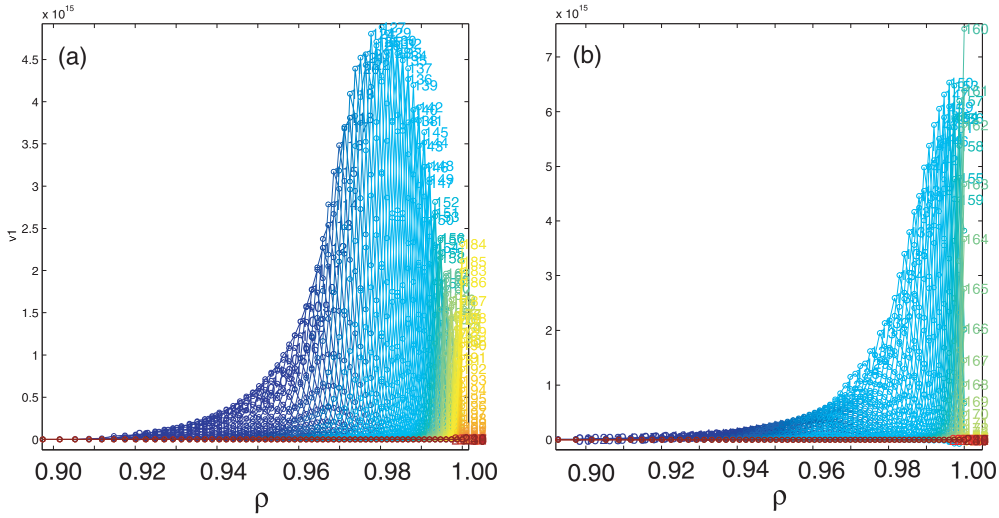

Figure 5. Eigenfunctions of $n = 40$ ballooning modes in situations with the edge of the pedestal $n = \infty$ ballooning unstable and the inner part of it second ballooning stable. (*a*) The edge unstable from $\psi = 0.935$ to $\psi = 1.000$, i.e. most of the pedestal unstable. (*b*) The edge unstable from $\psi = 0.990$ to $\psi = 1.000$.

density and temperature vary and are specified in each case. Similarly, the parameters defining the ELMs vary and are stated in each case. The ELM duration, however, is the same in all cases and is not mentioned explicitly each time. Both the type I and the type II ELMs are characterized by a rise time of 0.25 ms, a flat-top time of 0.5 ms and a fall time of 0.25 ms, yielding a total ELM duration of 1 ms. Also, the relative enhancement of particle diffusivity during the ELMs is generally only 10% of the relative enhancement of the ion and electron thermal conductivities in order to obtain a suitable balance of particle and heat dissipation. Finally, the effective charge in the simulations is $Z_{\text{eff}} = 2.0$.

7.1. Determination of optimal type II ELM width

In order to test the ELM model for mixed type I-II ELMy H-mode, simulations making use of the MISHKA results shown in figure 5 were performed. To be specific, a series of JETTO simulations was set up corresponding to a series of situations with a relatively wide inner part of the pedestal second ballooning stable and a relatively narrow edge part of it $n = \infty$ ballooning unstable. In these JETTO simulations, a Gaussian-shaped perturbation to transport having a characteristic width of 4.0 cm and being centred at $\rho = 0.965$ was used in the inner region of the ETB. With this choice of parameters, the perturbation representing a type I ELM resembled the eigenfunction in frame (*a*) in figure 5, as far as width and localization are considered. The inner region of the ETB extended from the top of the ETB at around $\rho = 0.94$ to $\rho = 0.98$ and the outer region from $\rho = 0.98$ to the separatrix. Here, the extent of the outer region corresponds roughly to the localization of the eigenfunction in frame (*b*) in figure 5 for a high-n ballooning mode in a situation with only the outermost edge of the pedestal unstable against $n = \infty$ ballooning modes. The ELM perturbation in the outer region was a Gaussian centred at $\rho = 0.995$ and its width was varied. The stability limits were $\tilde{\alpha}_{c,\text{I}} = 6.5$ in the inner region of the ETB and $\tilde{\alpha}_{c,\text{II}} = 2.5$ in the outer region. These values correspond roughly to the finite-n ballooning stability limit and the first stability limit, respectively. During the ELMs,

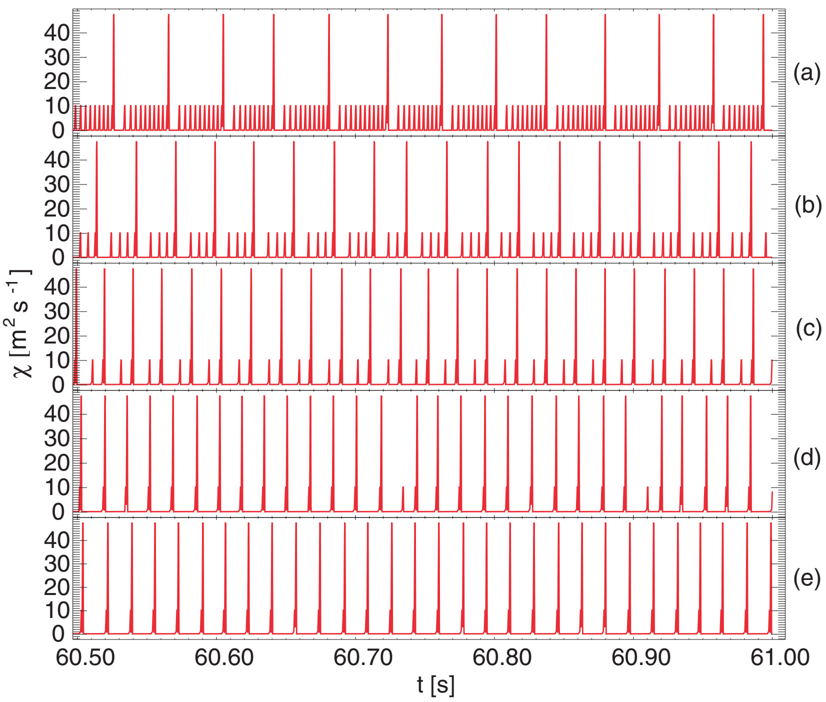

Figure 6. Ion thermal conductivity as a function of time in simulations of mixed type I-II ELMy H-mode with varying type II ELM width. Here, $\tilde{\alpha}_{c,\mathrm{I}} = 6.5$ in the inner region of the ETB and $\tilde{\alpha}_{c,\mathrm{II}} = 2.5$ in the outer region. The thermal conductivities are enhanced to a maximum level of $100\,\mathrm{m^2\,s^{-1}}$ and $10\,\mathrm{m^2\,s^{-1}}$, respectively, during the ELMs, the characteristic widths of the Gaussian-shaped perturbations are 4.0 cm and 1.0 cm, respectively and the centres of the perturbations are $\rho = 0.965$ and $\rho = 0.995$, respectively, in the inner and outer regions of the ETB. The type II ELM width varies as follows: (*a*) 1.0 cm, (*b*) 1.5 cm, (*c*) 2.0 cm, (*d*) 2.5 cm and (*e*) 3.0 cm.

ion and electron thermal conductivity was enhanced to a maximum level of $100\,\mathrm{m^2\,s^{-1}}$ and $10\,\mathrm{m^2\,s^{-1}}$ in the inner and outer regions of the ETB, respectively, reflecting the fact that type II ELMs are tiny compared with type I ELMs. These levels of transport can be compared with the level of thermal neoclassical transport, which is of the order of $0.2\,\mathrm{m^2\,s^{-1}}$. With this choice of parameters, each ELM type removes an appropriate amount of plasma thermal energy per ELM: around 7% of the total energy content in the case of type I ELMs and about two orders of magnitude less in the case of type II ELMs.

For comparison, a reference simulation of a pure type I ELMy H-mode was performed with the ELM representation resembling the eigenfunction in frame (*a*) in figure 5. In this simulation, the ETB was not split into two regions and, accordingly, a single critical pressure gradient $\tilde{\alpha}_c = 6.5$ was used, corresponding to the finite-n ballooning stability limit. The ELMs were represented by a single 4.0 cm wide Gaussian-shaped perturbation centred at $\rho = 0.97$ with the thermal conductivities amplified to a maximum level of $100\,\mathrm{m^2\,s^{-1}}$.

In the simulations with mixed type I-II ELMs, the characteristic width of the Gaussian-shaped perturbation in the outer pedestal region representing type II ELMs was varied from 1.0 cm to 3.0 cm in steps of 0.5 cm. It should be noted that the width of the perturbation itself varied considerably less than this, because the Gaussian was centred close to the separatrix. Figure 6, which contains time traces of the ion thermal conductivity at the magnetic surface $\rho = 0.99$ for each of these cases, shows how the frequencies of type I and type II ELMs are

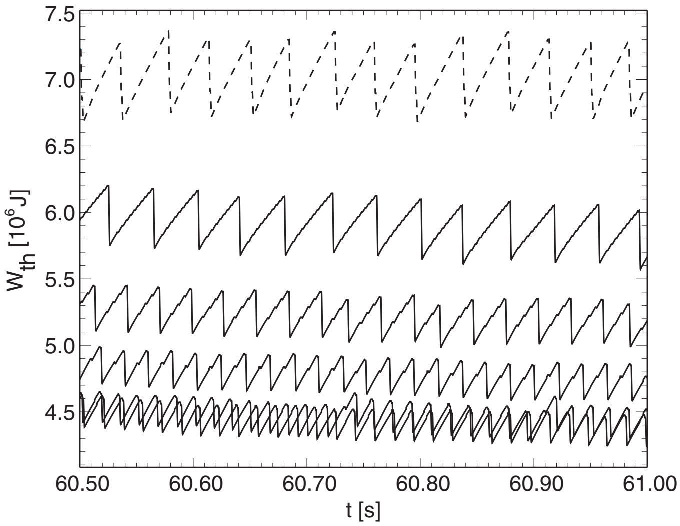

Figure 7. The thermal energy content as a function of time for the simulations in figure 6 with varying type II ELM width. The solid curves in the figure correspond to type II ELM widths of 1.0, 1.5, 2.0, 2.5 and 3.0 cm, from top to bottom. The dashed curve represents a reference simulation of a pure type I ELMy H-mode with simulation parameters corresponding to the series of simulations with mixed type I-II ELMs.

affected by the variation of the width of the type II ELMs. Showing characteristic time traces with frequent small-amplitude type II ELMs interrupted by occasional large-amplitude type I ELMs, the first few frames in the figure indicate that the new ELM model can qualitatively reproduce the dynamics of mixed type I-II ELMy H-mode with an appropriate choice of simulation parameters. The type II ELM frequency decreases with increasing width of the perturbations representing type II ELMs, because it takes a longer time for the edge pressure gradient to recover from stronger and wider perturbations, which cause a more significant depletion of the pedestal. Wide type II ELMs tend to flatten the pressure profile even inside the outer ETB region, so that the part of the pedestal with a steeper pressure gradient becomes narrower, thus prolonging the time it takes for the pressure gradient to build up sufficiently high again in the outer region. Nevertheless, the type I ELM frequency increases with increasing width of the type II ELMs, because the number of type II ELMs between each type I ELM decreases rapidly with the strength of the type II ELMs, whereby the total amount of energy removed between two consecutive type I ELMs decreases and the pressure gradient can build up to a type I ELM more quickly in the inner region of the pedestal.

It should be noted that the short ELM-free periods after type I ELM crashes before the onset of type II ELMs is a feature seen in some experimental discharges. In simulations with this ELM model, simulation parameters such as the type II ELM amplitude determine whether this feature is present or not. In the next subsection, an example with a smaller type II ELM amplitude resulting in an almost immediate onset of type II ELMs is shown.

Figure 7 shows time traces of the thermal energy content of the plasma for the simulations with different type II ELM widths. The thermal energy content, and thereby confinement, decreases with increasing type II ELM width. The explanation for this is again that the type II ELMs tend to flatten the pressure profile at the very edge, so that the pedestal effectively shrinks, whereby the pressure at the top of the pedestal drops and the energy stored in the pedestal decreases. Due to profile stiffness this translates into lower core temperatures and thus a smaller total energy content. For comparison, the energy content in the earlier described reference simulation of pure type I ELMy H-mode has also been plotted in figure 7.

With a type II ELM width of 1.0 cm, the thermal energy content of mixed type I-II ELMy H-mode is only about 15% lower than in the reference simulation of pure type I ELMy H-mode, as is often the case in experiments. With a type II ELM width of 1.5 cm, the deterioration of confinement with respect to type I ELMy H-mode is still consistent with that expected for a mixed type I-II ELMy H-mode. If the type II ELM width is 2.0 cm or more, the drop in confinement with respect to type I ELMy H-mode is already too large for a mixed type I-II ELMy H-mode. Moreover, as figure 6 shows, the number of type II ELMs between each type I ELM becomes unrealistically low for type II ELM widths above 1.5 cm. Hence, it can be concluded that the best results for mixed type I-II ELMy H-mode are obtained when the edge-localized perturbations representing type II ELMs have a width of approximately 1.5 cm or less. With this choice of type II ELM width and the perturbations centred at $\rho = 0.995$, the radial structure and localization of the type II ELMs closely match the eigenfunction in frame (*b*) in figure 5. In conclusion, ballooning modes become very edge localized in the high-n limit, if the very edge of the pedestal is infinite-n ballooning unstable and the rest of it second ballooning stable, and the dynamics of mixed type I-II ELMy H-mode is best reproduced, when the simulation model corresponds to this situation.

7.2. Comparison of mixed type I-II ELMy H-modes with other types of ELMy H-modes

As shown in the previous subsection, the simulation model described in section 5 can reproduce the experimental dynamics of mixed type I-II ELMy H-mode. Here, this is further demonstrated by comparing a simulation of mixed type I-II ELMy H-mode with reference simulations for pure type I and type II ELMy H-mode.

Figure 8 illustrates the ELM behaviour in a typical simulation of mixed type I-II ELMy H-mode, which will be compared with the reference simulations for other types of ELMy H-mode. Frame (*a*) in figure 8 shows the ion thermal conductivity at the magnetic surface $\rho = 0.995$ as a function of time, featuring the characteristic experimentally observed behaviour for mixed type I-II ELMy H-mode with quasi-continuous, small-amplitude type II ELMs interrupted by occasional large-amplitude type I ELMs. The simulation was performed with a high edge density resulting from a boundary condition of $n_0 = 3.33 \times 10^{19}\,\mathrm{m}^{-3}$ for the ion density at the separatrix, which is typical for mixed type I-II ELMy H-mode. As a result of the high separatrix density, the ion density at the top of the ETB and line averaged ion density in the simulation were also high: $n_{\mathrm{pedestal}} = 7.85 \times 10^{19}\,\mathrm{m}^{-3}$ and $n_{\mathrm{LA}} = 8.67 \times 10^{19}\,\mathrm{m}^{-3}$, respectively. Consistent with the high edge density, the boundary conditions for both the ion and electron temperatures at the separatrix were chosen to be modest, $T_0 = 30\,\mathrm{eV}$, and a high neutral beam heating power of $P = 16\,\mathrm{MW}$ was applied. The self-consistency of the boundary conditions in similar simulations has been studied in previous work on integrated modelling [8]. The critical pressure gradient had the values $\tilde{\alpha}_{c,\mathrm{I}} = 6.0$ and $\tilde{\alpha}_{c,\mathrm{II}} = 3.0$, typical for mixed type I-II ELMy H-mode, in the inner and outer regions of the ETB, respectively. The ion and electron thermal conductivities during the ELMs were amplified to maximum levels of $50\,\mathrm{m}^2\,\mathrm{s}^{-1}$ and $2\,\mathrm{m}^2\,\mathrm{s}^{-1}$, in the inner and outer regions of the ETB, respectively, corresponding to increases of roughly 250 and 10 times the level of thermal-ion neoclassical transport. Again, the ELM perturbations were Gaussians with characteristic widths of 4.0 cm and 1.0 cm centred at $\rho = 0.965$ and $\rho = 0.995$, in the inner and outer regions, respectively. Frame (*b*) in figure 8 shows the ion thermal conductivity at another flux surface, $\rho = 0.965$, providing, together with frame (*a*), some illustration of the localization of each ELM type. As shown in frame (*b*), the small type II ELMs do not influence transport in the inner region of the ETB at $\rho = 0.965$.

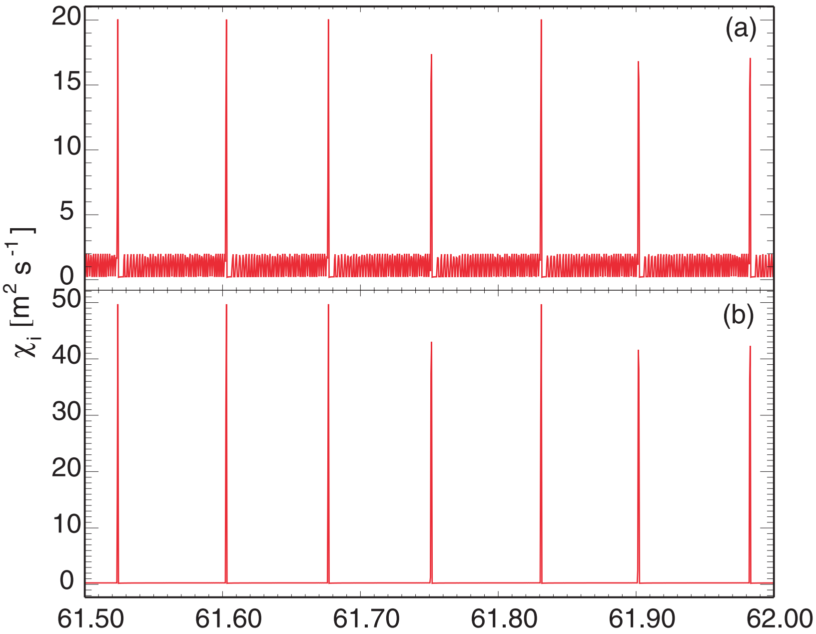

Figure 8. Ion thermal conductivity as a function of time in a typical simulation of mixed type I-II ELMy H-mode at (*a*) $\rho = 0.995$, (*b*) $\rho = 0.965$. Here, $\tilde{\alpha}_{c,\mathrm{I}} = 6.0$ in the inner region of the ETB and $\tilde{\alpha}_{c,\mathrm{II}} = 3.0$ in the outer region. Ion and electron thermal conductivity during the ELMs is enhanced to a maximum level of $50\,\mathrm{m^2\,s^{-1}}$ and $2\,\mathrm{m^2\,s^{-1}}$, in the inner and outer regions of the ETB, respectively. The characteristic widths of the Gaussian-shaped perturbations are 4.0 cm and 1.0 cm and the centres of the perturbations are at $\rho = 0.965$ and $\rho = 0.995$ in the inner and outer regions of the ETB, respectively.

At this radius, the time trace of the ion thermal conductivity looks like that of a pure type I ELMy H-mode, because the type II ELMs are completely localized further to the edge. It should be noted that the perturbations added to the transport coefficients due to the large type I ELMs are, in contrast, very significant in the whole pedestal. The relative levels of transport enhancement in the inner and outer pedestal regions can be discerned by comparing frames (*a*) and (*b*) in figure 8.

A reference type I ELMy H-mode simulation was performed using the value $\tilde{\alpha}_c = 6.0$ for the critical pressure gradient, i.e. the same value as for type I ELMs in the simulation of mixed type I-II ELMy H-mode. Transport during the ELMs was enhanced using a single Gaussian-shaped perturbation having the same amplitude, e.g. amplification factor about 250 for the thermal conductivities, and the same characteristic width, 4 cm, as the Gaussian-shaped perturbation for type I ELMs in the reference simulation of mixed type I-II ELMy H-mode. The ELM perturbation in the simulation of pure type I ELMy H-mode was centred at $\rho = 0.97$, i.e. slightly closer to the edge than in the simulation of mixed type I-II ELMy H-mode, in order to cover the edge properly. The simulation was performed at a lower density than the simulation of mixed type I-II ELMy H-mode in order to reflect the fact that the type I ELMy H-mode generally occurs in lower density ranges than mixed type I-II ELMy H-mode in experiments. Specifically, the separatrix ion density boundary condition was a modest $n_0 = 5 \times 10^{18}\,\mathrm{m^{-3}}$, resulting in a line averaged ion density of $n_{\mathrm{LA}} = 5.83 \times 10^{19}\,\mathrm{m^{-3}}$. The separatrix temperature boundary conditions were raised to $T_0 = 200\,\mathrm{eV}$ for both electrons and ions in order to keep the same pressure at the separatrix as in the simulation of mixed type I-II ELMy H-mode.

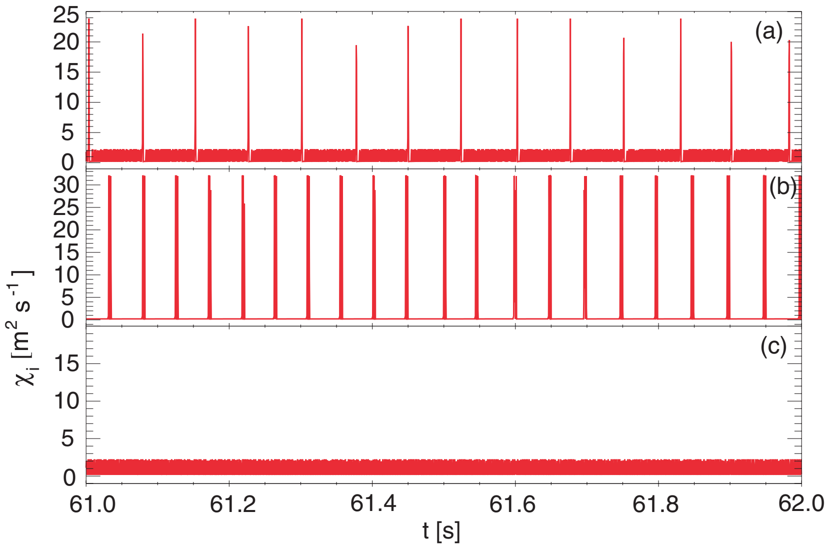

Figure 9. Ion thermal conductivity as a function of time at the magnetic surface $\rho = 0.99$ in three reference simulations of (*a*) mixed type I-II ELMy H-mode, (*b*) pure type I ELMy H-mode and (*c*) pure type II ELMy H-mode.

The neutral beam heating power was $P = 16\,\text{MW}$, i.e. the same as in the simulation of mixed type I-II ELMy H-mode, the high value being characteristic for the type I ELMy H-mode regime.

Finally, a reference simulation of pure type II ELMy H-mode was run using $\tilde{\alpha}_c = 3.0$ for the critical pressure gradient and a Gaussian having a characteristic width of 1.0 cm and being centred at $\rho = 0.995$ as ELM perturbation. The ELM amplitude was the same as for the type II ELMs in the reference simulation of mixed type I-II ELMy H-mode, i.e. the thermal conductivities were enhanced to $2\,\text{m}^2\,\text{s}^{-1}$. To put it simply, the type II ELM representation was taken unchanged from mixed type I-II ELMy H-mode simulation and the type I ELM representation was omitted completely. As in the simulation of mixed type I-II ELMy H-mode, the separatrix ion density boundary condition was $n_0 = 3.33 \times 10^{19}\,\text{m}^{-3}$, yielding a line averaged ion density of $n_{\text{LA}} = 8.67 \times 10^{19}\,\text{m}^{-3}$, and the separatrix temperature boundary conditions were $T_0 = 30\,\text{eV}$ for both electrons and ions. The neutral beam heating power was reduced to $P = 8\,\text{MW}$ in order to limit the pressure gradient in the inner part of the ETB to a level consistent with the pure type II ELMy H-mode. Without reducing the power in a simulation like this, the pressure gradient in the inner part of the pedestal would rise to a level at which type I ELMs should occur.

Figure 9 compares the ELM characteristics of the simulations of mixed type I-II, type I and type II ELMy H-mode shown in frames (*a*), (*b*) and (*c*), respectively. The plots are time traces of the ion thermal conductivity. It should be noted that the frequency of type I ELMs in the simulation of mixed type I-II ELMy H-mode is lower than the ELM frequency in the simulation of pure type I ELMy H-mode, which is consistent with experimental observations. The lower type I ELM frequency in mixed type I-II ELMy H-mode can be attributed mainly to two causes. For one thing, the energy and particle losses associated with the type II ELM activity between the type I ELMs increase the time it takes for the pressure gradient to recover from a type I ELM crash. Second, the higher edge density in the simulation of mixed type I-II

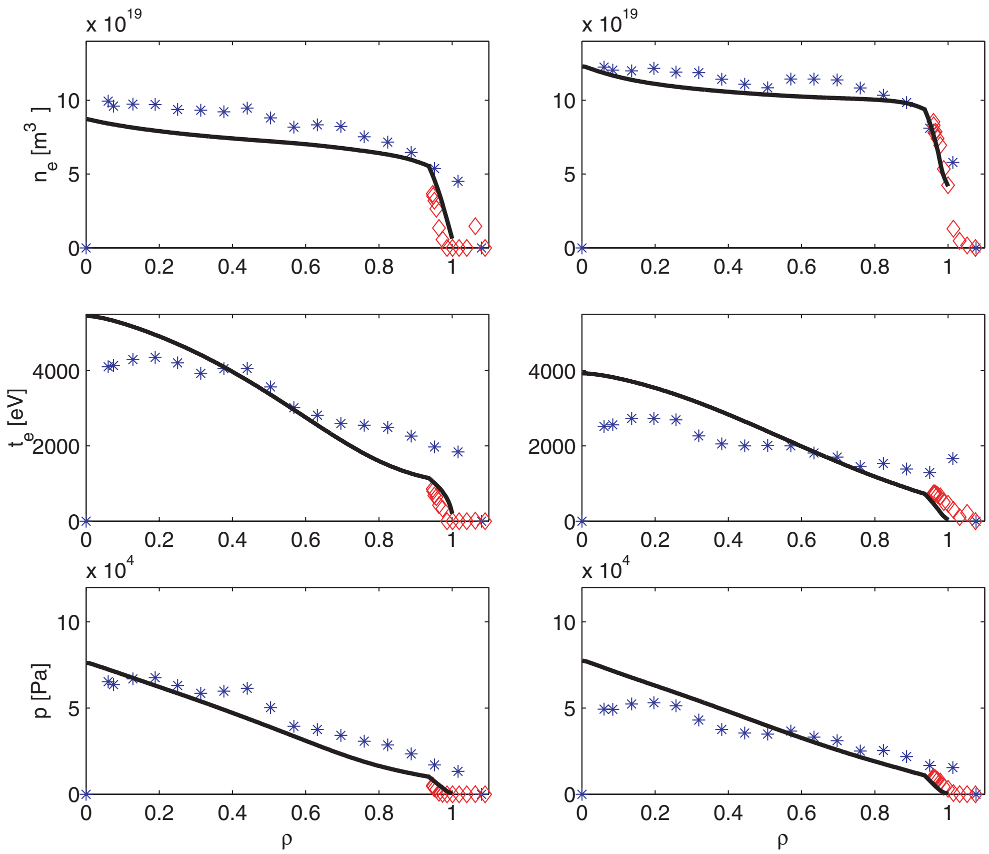

Figure 10. A comparison of plasma profiles obtained in simulations and experimental data. The left-hand column shows the electron density, electron temperature and electron pressure profiles in the reference simulation of type I ELMy H-mode together with experimental data from the type I ELMy H-mode JET discharge 53298. Similarly, the right-hand column shows the electron density, electron temperature and electron pressure profiles in the reference simulation of mixed type I-II ELMy H-mode together with experimental data from mixed type I-II ELMy H-mode JET discharge 53299. The plasma profiles from the simulations correspond to times shortly before type I ELMs, when the pressure gradient has evolved fully. The experimental data consists of edge and core Lidar (Thompson scattering) data.

ELMy H-mode results in greater neoclassical losses between the ELMs, which also increases the ELM recovery time.

The simulations of type I and mixed type I-II ELMy H-mode reproduce plasma profiles reasonably similar to those in experimental discharges. This is illustrated in figure 10, which compares the electron density, electron temperature and electron pressure profiles from the simulations of type I and mixed type I-II ELMy H-mode with experimental data from two JET discharges. Specifically, frames (*a*), (*b*) and (*c*) on the left-hand side of the figure compare plasma profiles from the type I ELMy H-mode simulation with electron density, electron temperature and electron pressure data from the type I ELMy H-mode discharge 53298 and frames (*d*), (*e*) and (*f*) on the right-hand side of the figure compare plasma profiles from mixed type I-II ELMy H-mode simulation with data from mixed type I-II ELMy H-mode discharge 53299. It should be noted that the simulations have e.g. the same magnetic configuration, the same total current and the same level of heating power as the chosen experimental discharges.

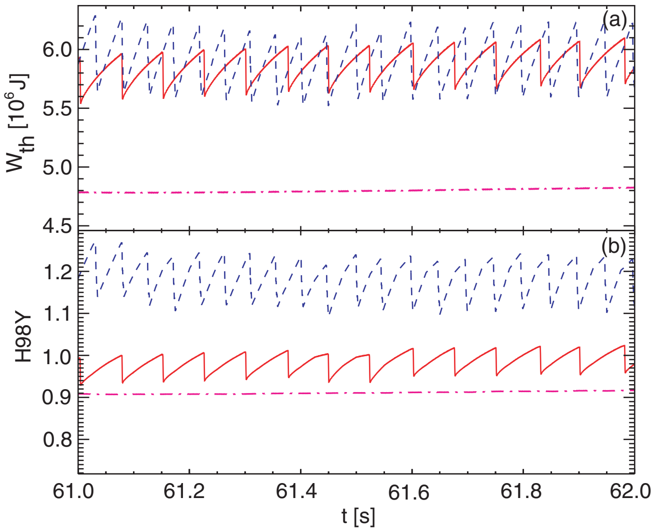

Figure 11. (*a*) Thermal energy content and (*b*) confinement factor H98Y as a function of time in three reference simulations of mixed type I-II ELMy H-mode (solid curve), pure type I ELMy H-mode (dashed curve) and pure type II ELMy H-mode (dash-dotted curve).

The plasma profiles from the simulations correspond to times shortly before type I ELMs, when the pressure gradient has evolved fully. The experimental data, which consist of edge and core Lidar (Thompson scattering) data, has been selected to correspond to a pre-ELM state as well as the existing data sampled at a low frequency permits. It should be noted that especially the data for the edge and pedestal region are associated with a rather large uncertainty. In particular, the traces made up by edge and core Lidar data points sometimes seem to give quite different pedestal heights and the edge Lidar data probably have a rather large artificial shift with respect to the plasma boundary, due to the difficulty of determining the location of the separatrix. Taking into account these factors and the fact that the simulations were not explicitly intended to reproduce the plasma profiles in any particular discharge, the match with the chosen JET discharges is reasonable. The fact that there is some mismatch between the experimental data and the calculated profiles in the deep core can be attributed to the Bohm/gyro-Bohm transport model used in JETTO and has nothing to with the ELM modelling scheme.

Figure 11 compares time traces of the thermal energy content, shown in frame (*a*), and the confinement factor H98Y [4], shown in frame (*b*), for the reference simulations of different types of ELMy H-mode. The simulation of pure type I ELMy H-mode features the highest level of thermal energy content and confinement. However, the simulation of mixed type I-II ELMy H-mode has only 3% lower pre-ELM thermal energy content than the reference simulation of pure type I ELMy H-mode. Measured in terms of confinement factor H98Y, the difference between the simulations is greater, about 20%, because the density, which plays a role in the H98Y scaling [4], is higher in the simulation of mixed type I-II ELMy H-mode. The result is consistent with the experimental observation that the pure type I ELMy H-mode often has slightly better plasma performance than mixed type I-II ELMy H-mode. The thermal energy content in the simulation with pure type II ELMs is about 23% lower than the pre-ELM thermal energy content in the simulation of pure type I ELMy H-mode and is thus slightly lower than in the simulation of mixed type I-II ELMy H-mode. The difference between type I and type II ELMy H-mode is about 25% measured in terms of the confinement factor H98Y. Since the

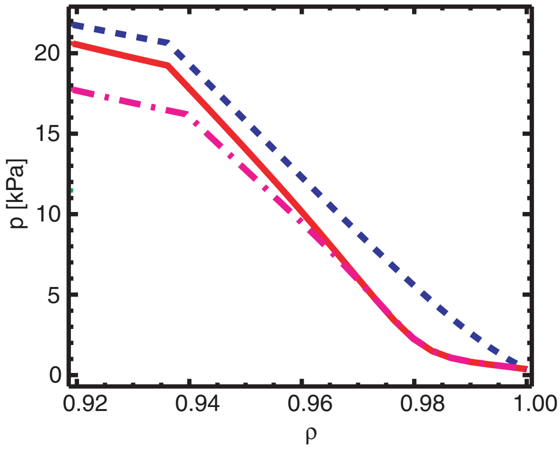

Figure 12. The pressure profiles in the near-pedestal region in three reference simulations of mixed type I-II ELMy H-mode (solid curve), pure type I ELMy H-mode (dashed curve) and pure type II ELMy H-mode (dash-dotted curve). In the cases of type I and mixed type I-II ELMy H-mode, the pressure profile corresponds to the situation shortly before a type I ELM.

pure type II ELMy H-mode has never been achieved at JET, the results obtained for this type of operation are difficult to verify.

In the simulation of pure type I ELMy H-mode with strong ELMs, each ELM removes about 9.5% of the plasma energy. In the simulation of mixed type I-II ELMy H-mode, the relative energy loss during the type I ELMs is slightly smaller as a result of the different density and temperature profiles. The type II ELMs, both in the simulation of mixed type I-II ELMy H-mode and in the simulation of pure type II ELMy H-mode remove only of the order of 0.1% of the thermal energy content per ELM. However, since the type II ELMs are very frequent, this is still enough to have a non-negligible influence on the recovery time between the type I ELMs in the simulation of mixed type I-II ELMy H-mode.

The different levels of thermal energy content and confinement in the simulations are a result of how the different ELM types shape the pedestal pressure profile. Due to profile stiffness, the temperature at the top of the pedestal determines the temperature level also in the core. Hence, the pedestal pressure profile effectively determines the level of total energy content. Figure 12 shows the pedestal pressure profiles in the simulations of type I, mixed type I-II and type II ELMy H-mode. In the cases of type I and mixed type I-II ELMy H-mode, the times used in the plot correspond to pre-type I ELM states, at which the pressure gradient has reached its maximum. The type I ELMy H-mode has the highest pressure at the top of the pedestal and the highest level of energy stored in the pedestal. The pedestal pressure gradient corresponds to $\tilde{\alpha}_c = 6.0$ specified for the simulation. In the simulation of mixed type I-II ELMy H-mode, the same level of pressure gradient is achieved in the inner region of the ETB. However, the pressure gradient in the outer region of the ETB is much flatter due to the condition $\tilde{\alpha}_{c,\mathrm{II}} = 3.0$ set for the type II ELMs, which effectively causes the pedestal to shrink with respect to the type I ELMy H-mode. Because of this, the pressure achieved at the top of the pedestal is lower than in type I ELMy H-modes. In the case of pure type II ELMy H-mode, the pressure profile in the region next to the separatrix is determined by the critical pressure gradient $\tilde{\alpha}_c = 3.0$ and corresponds roughly to the pressure profile in the outer region of the ETB in the case of mixed type I-II ELMy H-modes. Further inside the separatrix, no critical pressure gradient has been applied, whereby the pressure gradient has freely evolved to a steady-state level characteristic of the system. By increasing the heating power, the pressure gradient in this inner part of the ETB can be made steeper, leading to an increased total energy content. Hence, the level of thermal energy content for pure type II ELMy H-mode in figure 11 could easily be increased almost to the level achieved with mixed type I-II ELMy H-mode.

7.3. MHD stability

According to the model presented in section 4, the type I ELMy H-mode corresponds to a situation in which the discharge stays in the second ballooning stability region for all magnetic surfaces within the ETB. Similarly, mixed type I-II ELMy H-mode is proposed to be a situation with most of the pedestal second ballooning stable, but the very edge unstable against high-n ballooning modes. Here, MHD stability analysis performed on interpretative transport simulations is used to demonstrate that the model is in agreement with actual experimental situations. In interpretative simulations, experimental data are used for the density and temperature profiles, whereas the evolution of the current is predicted. MHD stability analysis is carried out when the simulation has reached a good steady state.

Here, JET discharge 55973 with type I ELMs is compared in terms of MHD stability with JET discharge 56044, which has mixed type I-II ELMs. The difference in the ELM characteristics of the two discharges is a result of their rather different experimental parameters. To be specific, discharges 55973 and 56044 have different toroidal magnetic fields, $B_0 = 2.40\,\mathrm{T}$ and $B_0 = 2.66\,\mathrm{T}$, respectively, on the axis; different plasma currents, $I = 2.0\,\mathrm{MA}$ and $I = 2.5\,\mathrm{MA}$, respectively; different levels of external neutral gas fuelling, $\Gamma = 0$ and $\Gamma = 5 \times 10^{22}\,\mathrm{s}^{-1}$ respectively; different line averaged densities, $n_{\mathrm{LA}} = 5.5 \times 10^{19}\,\mathrm{m}^{-3}$ and $n_{\mathrm{LA}} = 8.5 \times 10^{19}\,\mathrm{m}^{-3}$, respectively; and slightly different levels of external heating power, $P = 10\,\mathrm{MW}$ and $P = 11.5\,\mathrm{MW}$, respectively, by neutral beam injection. Edge and core Lidar (Thomson scattering) data for both temperature and density and electron cyclotron emission spectroscopy and charge exchange recombination spectroscopy data for the temperature were used in the interpretative JETTO simulations of the two pulses with the experimental data corresponding to times shortly before type I ELMs in the middle of the H-mode phases of the discharges. MHD stability analysis of the interpretative runs shows that discharge 55973 with type I ELMs is second ballooning stable for all magnetic surfaces within the ETB. Ballooning stability is uniquely determined by the finite-n ballooning stability limit. In the case of discharge 56044, most of the pedestal is second ballooning stable, but the edge outside $\rho = 0.983$ is infinite-n ballooning unstable. This is illustrated in figure 13, which compares MHD stability diagrams for the magnetic surface $\rho = 0.99$ for the interpretative simulations of the two discharges. The figure contains two stability diagrams in $\tilde{\alpha}$–s space with the mode numbers of the most unstable kink, peeling or ballooning modes ($n \leqslant 14$) and the $n = \infty$ ballooning unstable region indicated. This result obtained with MHD stability analysis performed directly on interpretative simulations using experimental profiles adds validity to the model for mixed type I-II ELMy H-mode. The fact that the operational point is located far inside the infinite-n ballooning unstable region in the case of discharge 56044 means that the plasma is deeply unstable at the edge and that this operational point cannot be sustained.

It should be noted that an ideal MHD version of the MISHKA code without shear flow or finite ion Larmor radius stabilization was used to calculate the results shown in figure 13. In reality, some of the modes with low growth rates given by the code might be stabilized by the finite gyro-radius effect of the ion diamagnetic drift frequency ω_i^*. Therefore, modes with growth rates lower than or equal to

$$\omega_i^* = \frac{m}{r}\frac{T_i}{e_i B_0}\frac{\mathrm{d}\ln p_i}{\mathrm{d}r}, \tag{7}$$

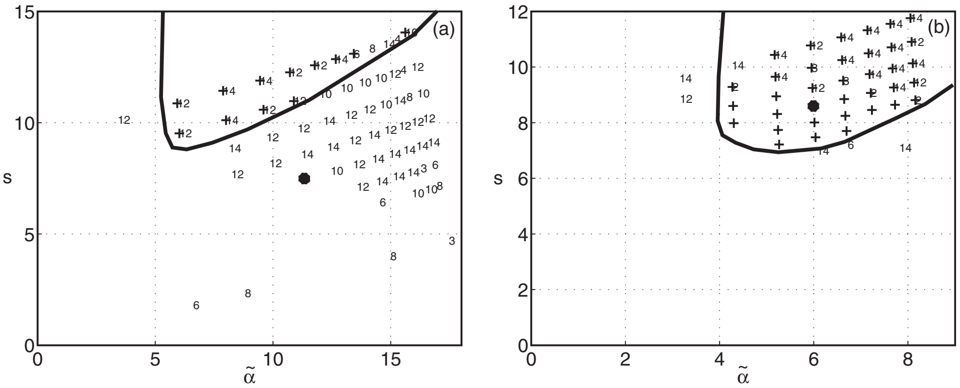

Figure 13. MHD stability diagrams indicating the mode numbers of the most unstable kink, peeling or ballooning modes for a number of locations in the $\tilde{\alpha}$–s space as well as the $n = \infty$ ballooning unstable region and the operational point for the magnetic surface $\rho = 0.99$ for two interpretative JETTO simulations of JET discharges: (*a*) 55973 with type I ELMs and (*b*) 56044 with mixed type I-II ELMs.

have been excluded from the plots in figure 13. Here, m is the poloidal mode number, r the local minor radius, T_i the ion temperature, e_i the ion charge, B_0 the toroidal magnetic field on the magnetic axis and p_i is the ion pressure. The ion diamagnetic drift frequency has been evaluated at the radius of largest amplitude of the MHD modes, where the instabilities can be assumed to be strongest.

8. Effect of the magnetic configuration on the occurrence of type II ELMs in H-mode plasmas

In section 2 it was noted that quasi-double-null magnetic configurations have been experimentally observed at ASDEX Upgrade to be favourable for the occurrence of type II ELMs in H-mode discharges. Type II ELMs have been observed both with single-null and quasi-double-null magnetic configurations, but quasi-double-null magnetic configurations seem to ease their occurrence. Here, the effect of the magnetic configuration on MHD stability and thus on ELM behaviour has been investigated by comparing interpretative JETTO simulations with single-null and quasi-double-null configurations.

In a first pair of simulations, JET discharge 53703, with a changing magnetic configuration was used in the analysis. In this discharge, the magnetic configuration changes from single-null via quasi-double-null to double-null in a few seconds. JETTO was run in the interpretative mode in two separate simulations, one of them with a good single-null configuration from discharge 53703 and the other one with a good quasi-double-null configuration from the same discharge. In order to include only the direct effect of the magnetic configuration on magnetic shear and edge stability and to exclude the indirect effect due to a difference in the plasma profiles resulting from the different magnetic configurations, exactly the same density and temperature profiles were used in both simulations. Figure 14 shows radial profiles of the magnetic shear in the two runs. As illustrated by the figure, the effect of the quasi-double-null configuration is to cause magnetic shear to increase strongly in the pedestal and its immediate vicinity. It should be noted that the magnetic shear is not calculated at the separatrix in JETTO and that the resolution of the equilibrium used in JETTO is not very good. Because of these limitations, the magnetic shear at the separatrix, instead of going towards infinity, looks very

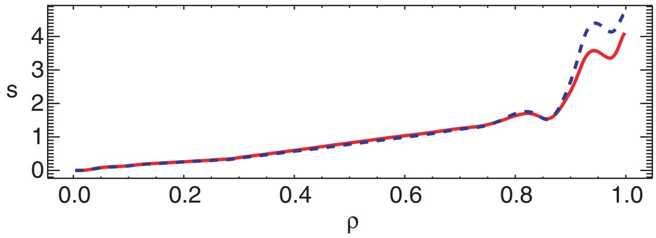

Figure 14. Radial profiles of magnetic shear in two interpretative JETTO simulations with different magnetic configurations. The solid curve corresponds to a simulation with a single-null magnetic configuration taken from JET discharge 53703 and the dashed curve to a simulation with a quasi-double-null magnetic configuration taken from the same discharge at a later time. The density and temperature profiles are exactly the same in both simulations.

finite in figure 14, which has been constructed directly from the JETTO output. The same considerations apply for other plots of magnetic shear shown later in this paper, as well. All the MHD stability diagrams, on the other hand, use the more accurately calculated magnetic shear given by HELENA.

MHD stability analysis was carried out on the simulations with different magnetic configurations. Despite the stronger magnetic shear in the simulation with the quasi-double-null magnetic configuration, ballooning stability is not qualitatively different in the two runs, because the infinite-n ballooning stability boundary moves in response to a change in the magnetic configuration. To be specific, both the stability boundary and the operational point are located at higher levels of magnetic shear with the quasi-double-null configuration than with the single-null configuration. The simulations were repeated with several different density profiles, but in each case the distance between the operational point and the infinite-n ballooning stability boundary was roughly the same with both configurations. With modest edge densities, both the simulation with the single-null magnetic configuration and the one with the quasi-double-null configuration are second ballooning stable for all magnetic surfaces within the ETB. With higher edge densities, the edge becomes infinite-n ballooning unstable in both simulations. Therefore, it can be concluded that a quasi-double-null magnetic configuration does not necessarily in itself directly make the edge more unstable against high-n ballooning modes than a single-null magnetic configuration, despite causing an increase in magnetic shear at the edge. Hence, the result indicates that a quasi-double-null magnetic configuration is not necessarily in itself more favourable for the occurrence of type II ELMs than a single-null magnetic configuration, according to this ELM model.

The favourability for type II ELMs attributed to quasi-double-null magnetic configurations seems to be due to the fact that quasi-double-null magnetic configurations are generally associated with higher average density than single-null configurations. Typically, a quasi-double-null JET discharge can have up to 20% higher average density than a single-null discharge with similar plasma parameters. As shown in section 4, the edge density affects ballooning stability very sensitively. Consequently, the comparison of single-null and quasi-double-null plasmas was repeated using actual experimental density and temperature profiles in interpretative JETTO simulations. JET discharges 56044 with a single-null magnetic configuration, already discussed in the previous section, and 56083 with a quasi-double-null configuration were selected for comparison. Since these two discharges otherwise have very similar plasma parameters, any difference in MHD stability between them should either directly or indirectly be due to the different magnetic configurations. In particular, the two discharges have the same toroidal magnetic field $B_0 = 2.66\,\mathrm{T}$ on the axis, the same plasma current $I = 2.5\,\mathrm{MA}$, the same level of external heating power $P = 12\,\mathrm{MW}$ by neutral

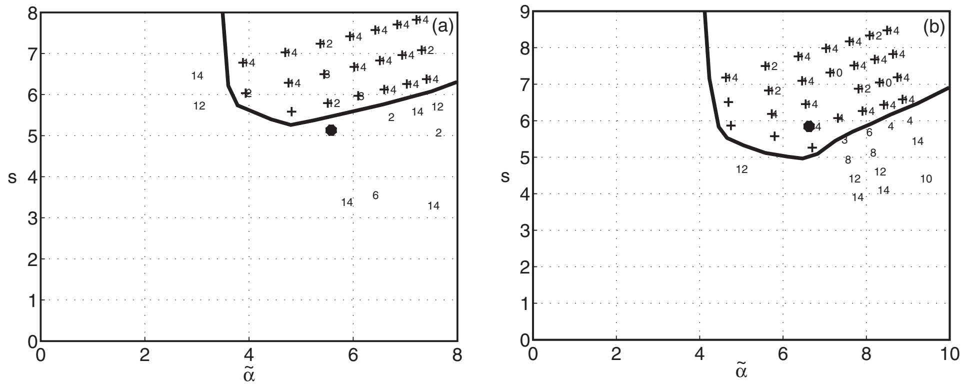

Figure 15. MHD stability diagrams indicating the mode numbers of the most unstable kink, peeling or ballooning modes for a number of locations in the $\tilde{\alpha}$–s space as well as the $n = \infty$ ballooning unstable region and the operational point for the magnetic surface $\rho = 0.98$ for two interpretative JETTO simulations of JET discharges: (*a*) 56044 with a single-null magnetic configuration and (*b*) 56083 with a quasi-double-null magnetic configuration.

beam injection and the same level of external neutral gas fuelling $\Gamma = 5 \times 10^{22}\,\mathrm{s}^{-1}$. The density is higher in discharge 56083 with the quasi-double-null configuration (line averaged density $n_{\mathrm{LA}} = 1.1 \times 10^{20}\,\mathrm{m}^{-3}$) than in discharge 56044 with the single-null configuration (line averaged density $n_{\mathrm{LA}} = 8.5 \times 10^{19}\,\mathrm{m}^{-3}$). The different magnetic configurations seem to be the only reason for the difference in density. The temperature and density profiles used in the simulations were constructed from edge and core Lidar, electron cyclotron emission spectroscopy and charge exchange recombination spectroscopy data taken from the middle of the H-mode phases of the discharges shortly before the onset of type I ELMs. Both discharges 56044 and 56083 have mixed type I-II ELMs. It would of course be of even greater interest to compare a type I ELMy H-mode discharge with a mixed type I-II ELMy H-mode discharge rather than two discharges with mixed type I-II ELMs, but suitable discharges differing only with respect to the magnetic configuration are not easy to find. The difference between type I and mixed type I-II ELMy H-mode discharges in terms of MHD stability has, however, already been demonstrated in the previous section. The comparison in this section still shows both qualitatively and quantitatively how the quasi-double-null configuration influences MHD stability in a way favourable for the occurrence of type II ELMs, either in mixed type I-II or in the pure type II ELMy H-mode regime.

The difference in MHD stability between discharges 56044 and 56083 is seen by comparing the magnetic surface $\rho = 0.98$, for which figure 15 shows MHD stability diagrams. As before, the mode numbers of the most unstable kink, peeling or ballooning modes ($n \leqslant 14$) and the $n = \infty$ ballooning unstable region are indicated in the $\tilde{\alpha}$–s space. Again, modes with growth rates lower than or equal to the ion diamagnetic drift frequency have been excluded, because the results were obtained assuming ideal MHD. Frame (*a*) shows that the simulation with the single-null magnetic configuration is stable against infinite-n ballooning modes at the magnetic surface $\rho = 0.98$. In the previous section, it was shown that the discharge is infinite-n ballooning unstable closer to the edge at $\rho = 0.99$, as expected for a mixed type I-II ELMy H-mode. Frame (*b*) reveals that the simulation with the quasi-double-null configuration is unstable against infinite-n ballooning modes at $\rho = 0.98$. In conclusion, both discharges are unstable against infinite-n ballooning modes at the edge, but the unstable region is slightly wider with the quasi-double-null magnetic configuration than with the single-null magnetic configuration. With the quasi-double-null magnetic configuration, the magnetic shear at the

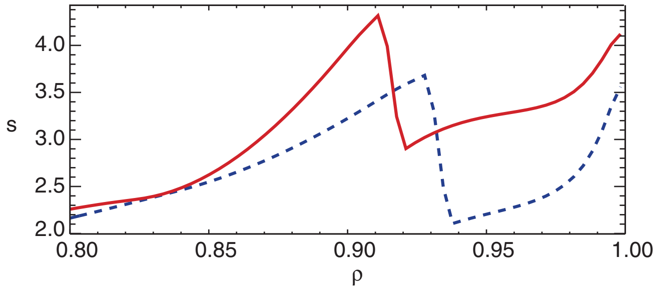

Figure 16. Radial profiles of magnetic shear, when the plasma has evolved for 1.0 s in H-mode, in two predictive JETTO simulations, the simulation parameters of which differ only with respect to the level of β_p. Here, the upper (solid) curve corresponds to $\beta_p = 2.6$ and the lower (dashed) curve to $\beta_p = 1.3$.

edge is stronger, which makes the edge more unstable against infinite-n ballooning modes, assuming that most of the pedestal is second ballooning stable. Hence, the present model, which associates type II ELMs with a situation with the outermost edge high-n ballooning unstable, indicates that a quasi-double-null magnetic configuration can be favourable for the occurrence of type II ELMs, either in mixed type I-II or in the pure type II ELMy H-mode regime. However, quasi-double-null magnetic configurations seem to be more favourable for the occurrence of type II ELMs than single-null magnetic configurations primarily because they are intrinsically associated with higher edge (and average) densities.

9. Effect of β_p on the occurrence of type II ELMs in H-mode plasmas

As noted in section 2, high β_p has been experimentally observed e.g. at JT-60U, to be favourable for the occurrence of type II ELMs in H-mode plasmas, both in mixed type I-II and pure type II ELMy H-mode regimes. The effect of β_p on infinite-n ballooning stability has been studied by running HELENA on a series of predictive JETTO simulations with varying β_p. Since the influence of β_p is subtle, it is easier to demonstrate the effect through predictive modelling, which allows suitable cases to be constructed, than to try to find discharges differing only with respect to β_p and ELM type. In predictive simulations, different levels of β_p can be obtained, e.g. by adding different fractions of suprathermal energy content on top of the thermal energy content in the pressure used when solving the Grad–Shafranov equation in recalculations of the equilibrium with JETTO's equilibrium solver ESCO. Here, the effect of β_p is demonstrated using two predictive simulations with the nominal pressure multiplied by 1.2 and 2.4, respectively, in the equilibrium recalculations. In the latter simulation, the effective level of β_p is, consequently, two times higher than in the former one or about $\beta_p = 2.6$ compared to $\beta_p = 1.3$, the values evolving slightly with time. In both cases, the simulations were first run for 0.5 s in L-mode, whereupon the plasma was allowed to evolve in H-mode towards a steady state without imposing ELMs on it. The boundary conditions were $n_0 = 2.9 \times 10^{19}\,\mathrm{m}^{-3}$ for the ion density at the separatrix and $T_0 = 100\,\mathrm{eV}$ for the electron and ion temperatures at the separatrix, and the total plasma current was $I = 2.5\,\mathrm{MA}$. Infinite-n ballooning stability analysis was carried out 1.0 s after the transition to the H-mode, when the pressure gradient had evolved to a level roughly corresponding to the finite-n ballooning stability limit.

Figure 16 shows radial profiles of magnetic shear at the times chosen for MHD stability analysis in the two simulations with low and high β_p. It is evident that magnetic shear within the

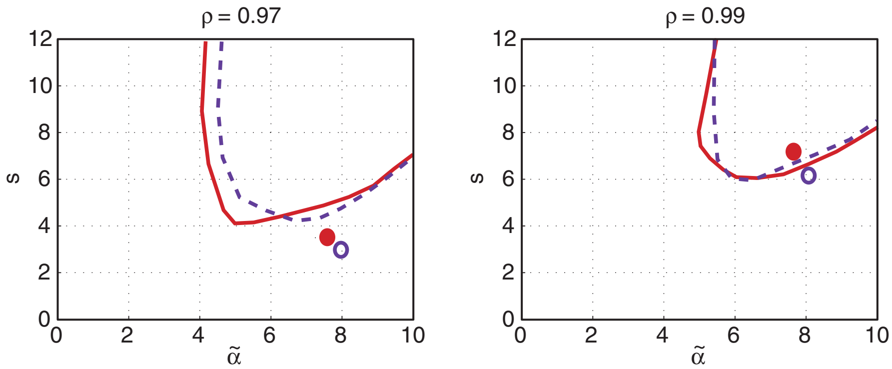

Figure 17. Infinite-n ballooning stability diagrams for the two predictive JETTO simulations with $\beta_p \approx 1.3$ (dashed curve and hollow point) and $\beta_p \approx 2.6$ (solid curve and solid point) showing the $n = \infty$ ballooning stability boundary and the operational point for the magnetic surfaces $\rho = 0.97$ and $\rho = 0.99$.

ETB increases strongly with β_p, which implies that the edge is more unstable in the simulation with high β_p. It should be noted that the width of the ETB increases in terms of the toroidal flux co-ordinate ρ, with increasing β_p. This effect is due to the Shafranov shift of the flux surfaces, which increases with increasing β_p. The absolute width of the ETB does not increase, since the magnetic surfaces only become more closely packed at the outer side of the plasma.

The results of infinite-n ballooning stability analysis for the low and high β_p simulations are illustrated in figure 17, which shows $n = \infty$ ballooning stability diagrams with the normalized pressure gradient $\tilde{\alpha}$ on the horizontal axis and magnetic shear s on the vertical axis for two different flux surfaces, $\rho = 0.97$ and $\rho = 0.99$. The results have been obtained by running HELENA on a series of equilibria with systematically changing perturbations applied to the edge pressure gradient and edge current. The operational point corresponding to the unperturbed equilibrium is shown for each case. In the simulation with the lower value of β_p, the operational point is located in the second ballooning stability region for both $\rho = 0.97$ and $\rho = 0.99$. In fact, the pedestal is completely second ballooning stable in this case. In the simulation with the higher value of β_p, the situation is qualitatively different. As shown in figure 17, $\rho = 0.97$ is second ballooning stable, whereas $\rho = 0.99$ is infinite-n ballooning unstable. More precisely, the pedestal is unstable from $\rho = 0.988$ to the separatrix.

The qualitative difference in high-n ballooning stability between the two analysed simulations with different β_p is due to the fact that magnetic shear at the edge is higher in the simulation with higher β_p. According to the present model, the situation with the lower β_p corresponds to a pure type I ELMy H-mode, whereas the situation with the higher β_p corresponds to a mixed type I-II ELMy H-mode. Because the predictive simulations analysed here essentially differ only with respect to β_p, the difference in ballooning stability can be attributed entirely to this parameter and the modelling thus implies that high β_p is favourable for the occurrence of type II ELMs in H-mode plasmas by making the outermost edge of the plasma more unstable against high-n ballooning modes.

10. Effect of the edge safety factor on the occurrence of type II ELMs in H-mode plasmas

In section 2, it was noted that situations with a combination of high edge safety factor q and high triangularity δ have been found to be favourable for type II ELMs in experiments. Here,

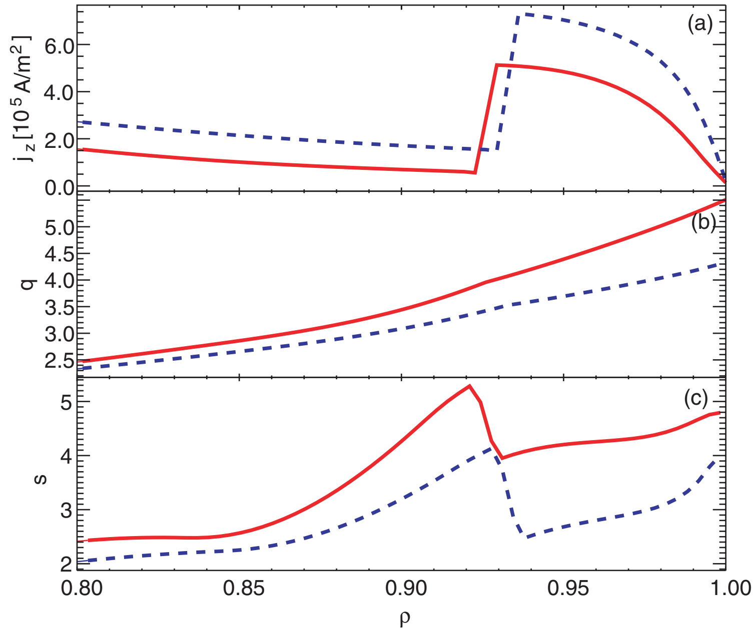

Figure 18. Radial profiles of (*a*) the total current density, (*b*) the safety factor and (*c*) magnetic shear, when the plasma has evolved for 0.5 s in H-mode, in two predictive JETTO simulations, the simulation parameters of which differ only with respect to the total current. Here, the solid curves correspond to the total current $I = 2.1$ MA and the dashed curves to $I = 2.5$ MA.

the effects of the edge safety factor and triangularity are investigated separately, starting with the effect of the edge safety factor in this section. For simplicity, the same approach as in the preceding section discussing the effect of β_p is followed.

To begin with, two predictive JETTO simulations with different q profiles were constructed by varying the boundary condition for the current. The plasma was allowed to evolve towards a steady state without imposing ELMs on it. Infinite-n ballooning stability analysis was carried out when the pressure gradient had evolved to a level roughly corresponding to the finite-n ballooning stability limit. Figure 18 shows the radial profiles of the total current density in frame (*a*), of the safety factor in frame (*b*) and of magnetic shear in frame (*c*) for two of the predictive JETTO simulations with different levels of edge safety factor. It should be noted that, like the magnetic shear, the safety factor is not calculated at the separatrix in JETTO, which is the reason why q looks rather low at the separatrix instead of going towards infinity. The total current was $I = 2.1$ MA and $I = 2.5$ MA in the high- and low-q simulations, respectively. In both cases, the boundary conditions were $n_0 = 2.5 \times 10^{19}$ m^{-3} for the ion density at the separatrix and $T_0 = 100$ eV for the electron and ion temperatures at the separatrix. With these boundary conditions, the safety factor takes the values $q_{95} = 4.25$ and $q_{95} = 3.69$ at $\psi = 0.95$ for $I = 2.1$ MA and $I = 2.5$ MA, respectively, at the time chosen for ballooning stability analysis, i.e. when the pressure gradient has evolved to a level roughly corresponding to the finite-n ballooning stability limit. It is evident that magnetic shear at the edge increases with increasing edge safety factor. As in the analysis in the preceding section, the increase in magnetic shear tends to push the operational point at the outermost magnetic surfaces into the $n = \infty$ ballooning unstable region, i.e. create a situation corresponding to an H-mode with type II ELMs according to the present model.

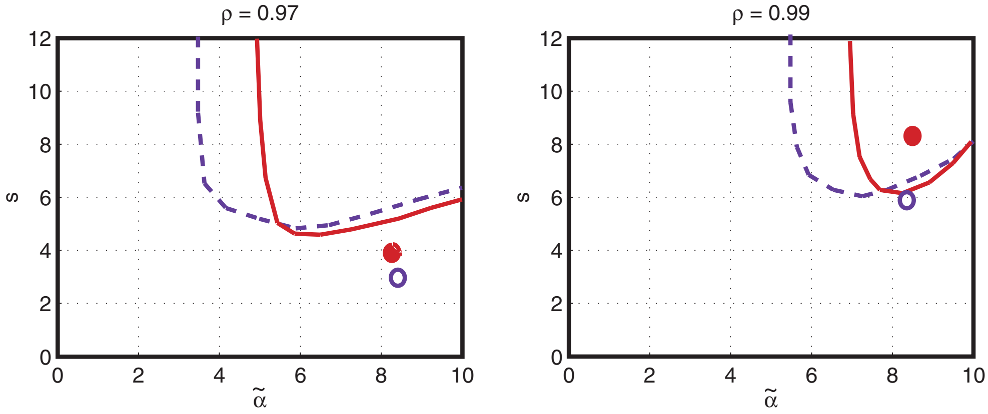

Figure 19. Infinite-n ballooning stability diagrams for the two predictive JETTO simulations with different total currents translating into $q_{95} = 3.69$ (dashed curve and hollow point) and $q_{95} = 4.25$ (solid curve and solid point). The diagrams show the $n = \infty$ ballooning stability boundary and the operational point for the magnetic surfaces $\rho = 0.97$ and $\rho = 0.99$.

Figure 19 illustrates the results of $n = \infty$ ballooning stability analysis for the situations with $q_{95} = 3.69$ and $q_{95} = 4.25$. Stability diagrams are again shown for the magnetic surfaces $\rho = 0.97$ and $\rho = 0.99$, as in the preceding section on the effect of β_p. In the case with lower q, both $\rho = 0.97$ and $\rho = 0.99$ are second ballooning stable flux surfaces. In fact, the operational point stays in the second ballooning stability region for all magnetic surfaces within the ETB, implying that the simulation in terms of high-n ballooning stability corresponds to a pure type I ELMy H-mode. In the case with the higher q, $\rho = 0.97$ is second ballooning stable, whereas $\rho = 0.99$ is infinite-n ballooning unstable. To be specific, the pedestal is infinite-n ballooning unstable from $\rho = 0.985$ to the separatrix. According to the model used in this paper, the simulation with higher q corresponds to a plasma with type II ELMs. Hence, the overall result from the simulations under consideration is that high q at the edge seems to be favourable for the occurrence of type II ELMs.

11. Effect of triangularity on the occurrence of type II ELMs in H-mode plasmas

In this section, the effect of triangularity on the ELM characteristics is examined separately, in the same way as the effect of the edge safety factor was examined in the preceding section. Using a momentum approximation for an up–down symmetric plasma boundary, three predictive JETTO simulations with triangularities $\delta = 0.3$, $\delta = 0.4$ and $\delta = 0.5$ have been performed. By changing the minor radius slightly, the plasma volume was kept the same in all three cases. Since changing the minor radius affects the q profile, the boundary condition for the total current was also slightly different in each case in order to keep the level of the edge safety factor constant. The separatrix ion density was $n_0 = 2.3 \times 10^{19}\,\mathrm{m}^{-3}$ and the ion and electron temperatures at the separatrix, $T_0 = 100\,\mathrm{eV}$ in each of the cases. Figure 20 shows the radial profiles of magnetic shear in the three simulations. As expected, magnetic shear at the edge increases with increasing triangularity. Infinite-n ballooning stability analysis was performed on the simulations. It turns out that all three simulations are qualitatively very similar with respect to high-n ballooning stability, despite the increase in magnetic shear with triangularity. The explanation for this is that the stability boundary evolves strongly as a function of the triangularity. Due to this effect, the simulations do not become more high-n

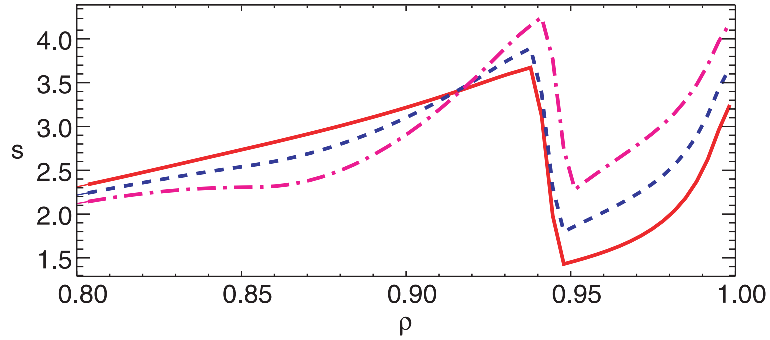

Figure 20. Radial profiles of magnetic shear, when the plasma has evolved for 0.5 s in H-mode, in three predictive JETTO simulations, the simulation parameters of which differ only with respect to the triangularity. Here, the solid curve corresponds to $\delta = 0.3$, the dashed curve to $\delta = 0.4$ and the dash-dotted curve to $\delta = 0.5$.

ballooning unstable at the edge with increasing triangularity. This result could imply that the edge safety factor might be more important than triangularity for obtaining plasma conditions favourable for the occurrence of type II ELMs. Since high triangularity clearly provides the necessary increase in magnetic shear very efficiently, it is understandable that this feature still seems to be beneficial for operation with type II ELMs. However, there is a more plausible explanation for the result obtained in this section: an increase in triangularity usually leads to an increase in edge density, in the same way as a transition from a single-null to a quasi-double-null magnetic configuration, and this has been shown to affect ballooning stability sensitively. The effect on the density is not taken into account in the predictive simulations. Taking into account the density increase associated with high triangularity, it becomes straightforward to show that increasing triangularity makes the edge more unstable against high-n ballooning modes, which according to the present model shows high triangularity to be favourable for the occurrence of type II ELMs. This result would also be consistent with the experimental observation that both the edge safety factor and the triangularity influence the occurrence of type II ELMs.

12. Summary and discussion

Type II ELMs, which offer rather good confinement properties and produce only modest heat loads on the divertor plates, are of interest for the operation of tokamak devices. Experimentally, mixed type I-II and pure type II ELMy H-modes have been observed in a number of situations: in discharges with relatively strong external neutral gas puffing, with quasi-double-null magnetic configurations, with high β_p and with combinations of high edge safety factor and high triangularity.

Exemplified by transport simulations differing with respect to the level of external neutral gas puffing, simple models making use of the often expressed idea that type I and type II ELMs are associated with medium- and high-n ballooning modes, respectively, have been introduced. Type I ELMs are proposed to be caused by violations of the finite-n ballooning stability limit, whereas type II ELMs are suggested to occur when high-n ballooning stability is violated at the very edge of the plasma. The models for type I and type II ELMs have been combined into an improved scheme for modelling of mixed type I-II ELMy H-mode, which has been implemented into the 1.5D core transport code JETTO together with simple schemes for the modelling of pure type I and type II ELMy H-modes based on the same ideas. In particular, the ETB has been divided into an inner and an outer region, in which stability for type I and type II ELMs, respectively, is evaluated using appropriate limits for the pressure gradient derived from MHD stability analysis. Transport during the ELMs is enhanced by edge-localized radially Gaussian-shaped perturbations to the transport coefficients and type I and type II ELMs are represented by perturbations with different widths and amplitudes. The approach has been given some justification from theory and numerical analysis.

As shown in this paper, it is possible to qualitatively reproduce the experimental dynamics of mixed type I-II ELMy in predictive transport simulations with the ELM modelling scheme. The ELM model also provides a plausible way to explain why some special effects and situations such as strong gas puffing, a quasi-double-null magnetic configuration, high β_p and high edge safety factor and high triangularity can be favourable for mixed type I-II and pure type II ELMy H-mode. By performing MHD stability analysis on interpretative and predictive JETTO simulations, it has been shown that these situations lead to a strong increase in magnetic shear at the very edge of the plasma, which can cause this outermost region to become high-n ballooning unstable, thereby effectively returning the operational point back to the first ballooning stability region.

A general observation in this study is that the operational ranges for mixed type I-II and pure type II ELMy H-mode are rather narrow in terms of e.g. density, power, poloidal β and edge safety factor, which is consistent with experiments. For instance, a slight increase in density, or equivalently a slight decrease in power, causes a mixed type I-II ELMy H-mode to transfer into a type III ELMy H-mode regime with poor confinement. Infinite-n ballooning stability analysis performed on the different scenarios discussed in this paper indicates that the edge density, which can be controlled by, e.g. external gas puffing, is the most important parameter controlling the transitions between different types of ELMy H-mode. Parameters such as β_p and the edge safety factor clearly play a role in determining the ELM type, but only in limited density ranges. In many of the examples used in this paper, the edge density has deliberately been chosen so that other effects become apparent.

The modelling does not unambiguously show that quasi-double-null magnetic configurations and high triangularity are, in themselves, favourable for the occurrence of type II ELMs. Nevertheless, it has been shown that quasi-double-null magnetic configurations and high triangularity lead to a strong increase in magnetic shear at the edge. In the predictive simulations, which do not take into account the effect of the magnetic configuration and plasma shaping on the density profile, the operational point does not become more unstable despite the strong increase in magnetic shear, because the $n = \infty$ ballooning unstable region shrinks significantly with the increasing magnetic shear. Quasi-double-null magnetic configurations and high triangularity seem to be more favourable for the occurrence of type II ELMs, primarily because they result in a higher edge (and average) density than single-null magnetic configurations and low triangularity, respectively. Type II ELMs have been experimentally observed (among other situations) for combinations of high edge safety factor and high triangularity. The result obtained here could also indicate that the edge safety factor might be more important than the triangularity as far as favourability for type II ELMs is concerned.

Acknowledgment

This work has been performed under the European Fusion Development Agreement.

References

[1] Chankin A V and Saibene G 1999 *Plasma Phys. Control. Fusion* **41** 913
[2] Connor J W 1997 *Plasma Phys. Control. Fusion* **40** 531
[3] Suttrop W 1999 *Plasma Phys. Control. Fusion* **42** A1
[4] ITER Physics Experts Groups on Confinement and Confinement and Transport Modelling and Database, ITER Physics Basis Editors, ITER EDA 1999 *Nucl. Fusion* **39** 2175
[5] Ferron J R *et al* 2000 *Nucl. Fusion* **40** 1411
[6] Ferron J R *et al* 2000 *Phys. Plasmas* **7** 1976
[7] Snyder P B *et al* 2002 *Phys. Plasmas* **9** 2037
[8] Lönnroth J-S *et al* 2003 *Plasma Phys. Control. Fusion* **45** 1689
[9] Lönnroth J-S *et al* 2004 *Plasma Phys. Control. Fusion* **46** at press
[10] Saibene G *et al* 2001 *Proc. 28th EPS Conf. on Plasma Physics and Controlled Fusion (Madeira, Portugal, 18–22 June 2001)*
[11] Kamada Y *et al* 2002 *Plasma Phys. Control. Fusion* **44** A279
[12] Kamada Y *et al* 2000 *Plasma Phys. Control. Fusion* **42** A247
[13] Lao L *et al* 2001 *Nucl. Fusion* **41** 295
[14] Stober J *et al* 2001 *Nucl. Fusion* **41** 1123
[15] Gruber O *et al* 2002 *Proc. 19th IAEA Conf. (Lyon, France)*
[16] Cennachi G and Taroni A 1988 JET-IR(88)03
[17] Mikhailovskii A B *et al* 1997 *Plasma Phys. Rep.* **23** 844
[18] Erba M *et al* 1997 *Plasma Phys. Control. Fusion* **39** 261
[19] Houlberg W A, Shaing K C, Hirshman S P and Zarnstorff M C 1997 *Phys. Plasmas* **4** 3231
[20] Onjun T, Kritz A, Bateman G and Parail V 2003 *Proc. 11th Int. Congress on Plasma Physics (Sydney, Australia, 15–19 July 2002)*
[21] Onjun T, Bateman G, Kritz A H and Hammet G 2002 *Phys. Plasmas* **9** 5018
[22] Huysmans G T A, Hender T and Alper B 1998 *Nucl. Fusion* **38** 179
[23] Connor J W, Hastie R J, Wilson H R and Miller R L 1998 *Phys. Plasmas* **5** 2687
[24] Rogers B N and Drake J F 1999 *Phys. Plasmas* **6** 2797
[25] Hastie R J, Catto P J and Ramos J J 2000 *Phys. Plasmas* **7** 4561
[26] Connor J W, Hastie R J and Taylor J B 1979 *Proc. R. Soc.* A **365** 1
[27] Huysmans G T A, Sharapov S E, Mikhailovskii A B and Kerner W 2001 *Phys. Plasmas* **10** 4292
[28] Saarelma S, Günter S and Horton L D 2003 *Nucl. Fusion* **43** 262